Bacterial and host enzymes modulate the inflammatory response produced by the peptidoglycan of the Lyme disease agent

Joshua W. McCausland[1,2,3] †, Zachary A. Kloos[4] †, Irnov Irnov[1,3] †, Nicole D. Sonnert[4,5] †, Junhui Zhou[6], Rachel Putnick[6], Elizabeth A. Mueller[1,2,3], Allen C. Steere[8], Noah W. Palm[5], Catherine L. Grimes[6], and Christine Jacobs-Wagner[1,2,3,9,] ✉

[1]Sarafan ChEM-H Institute, Stanford University, Stanford, CA, USA
[2]Department of Biology, Stanford University, Stanford, CA, USA
[3]Howard Hughes Medical Institute, Stanford University, Stanford, CA, USA
[4]Microbiology Program, Yale University, West Haven, Connecticut, USA
[5]Department of Immunology, Yale University School of Medicine, New Haven, CT, USA
[6]Department of Chemistry and Biochemistry, University of Delaware, Neward, DE
[7]Center for Immunology and Inflammatory Diseases, Massachusetts General Hospital and Harvard Medical School, Boston, MA, USA
[8]Department of Microbiology and Immunology, Stanford University School of Medicine, Stanford, CA, USA

The spirochete *Borrelia burgdorferi* causes Lyme disease. In some patients, an excessive, dysregulated proinflammatory immune response can develop in joints leading to persistent arthritis even after antibiotic therapy. In such patients, persistence of antigenic *B. burgdorferi* peptidoglycan (PG^{Bb}) fragments within joint tissues may contribute to immunopathogenesis pre- and post-antibiotic treatment. In live *B. burgdorferi* cells, the outer membrane shields the polymeric PG^{Bb} sacculus from exposure to the immune system. However, unlike most diderm bacteria, *B. burgdorferi* releases PG^{Bb} turnover products into its environment due to the absence of recycling activity. In this study, we identified the released PG^{Bb} fragments using a mass spectrometry-based approach. By characterizing the L,D-carboxypeptidase activity of *B. burgdorferi* protein BB0605 (renamed DacA), we found that PG^{Bb} turnover largely occurs at sites of PG^{Bb} synthesis. In parallel, we demonstrated that the lytic transglycosylase activity associated with BB0259 (renamed MltS) releases PG^{Bb} fragments with 1,6-anhydro bond on their *N*-acetylmuramyl residues. Stimulation of human cell lines with various synthetic PG^{Bb} fragments revealed that 1,6-anhydromuramyl-containing PG^{Bb} fragments are poor inducers of a NOD2-dependent immune response relative to their hydrated counterparts found in the polymeric PG^{Bb} isolated from dead bacteria. We also showed that the activity of the human *N*-acetylmuramyl-L-alanine amidase PGLYRP2, which reduces the immunogenicity of PG^{Bb} material, is low in joint (synovial) fluids relative to serum. Altogether, our findings suggest that MltS activity helps *B. burgdorferi* evade PG-based immune detection by NOD2 during growth despite shedding PG^{Bb} fragments and that PG^{Bb}-induced immunopathology likely results from host sensing of PG^{Bb} material from dead (lysed) spirochetes. Additionally, our results suggest the possibility that natural variation in PGLYRP2 activity may contribute to differences in susceptibility to PG-induced inflammation across tissues and individuals.

Correspondence: ***jacobs-wagner@stanford.edu***

†: These authors contributed equally to this work.

Author summary

During bacterial infection, the presence of peptidoglycan–a polymeric element of bacterial cell walls–triggers a host inflammatory response. Although generally protective during acute phases, inflammation, when chronic, can contribute to disease development. Recent work has suggested that the persistence of pro-inflammatory peptidoglycan derived from the Lyme disease spirochete *Borrelia burgdorferi* in joints may contribute to persistent arthritis in some patients despite appropriate antibiotic therapy. Interestingly, *B. burgdorferi* sheds peptidoglycan turnover products into the environment during growth. Here, we show that these shed products from live spirochetes are poor effectors of an immune response by the human NOD2 immune receptor due to the formation of an anhydro bond on the *N*-acetyl-muramic residue during peptidoglycan hydrolysis by a *B. burgdorferi* lytic transglycosylase. We also show that human *N*-acetylmuramyl-L-alanine amidase activity, which abrogates the NOD2-dependent response to the immunogenic peptidoglycan isolated from lysed *B. burgdorferi* cells, is low in human joint fluids relative to serum. Based on our findings, we propose that immunopathogenesis by peptidoglycan material more likely derives from lysed spirochetes (killed by an immune attack or antibiotics) than live ones and that the level of human peptidoglycan hydrolytic enzymes across tissues and individuals influences susceptibility to chronic inflammation.

Introduction

Lyme disease is the most prevalent and fastest-growing vector-borne disease in the United States and Northern Europe (1–4). It is caused by *Borrelia burgdorferi*, a spirochete that is transmitted by *Ixodes* ticks. This pathogen circulates in nature through transmission and persistence in vertebrate reservoirs including rodents, birds, and lizards (5). Infection in humans is often apparent by the presence of a slowly expanding skin lesion at the site of the tick bite. In the absence of appropriate diagnosis and antibiotic

therapy, *B. burgdorferi* can disseminate widely to extracutaneous tissues, producing multisystem clinical manifestations such as flu-like symptoms, meningitis, carditis, and often arthritis, a late disease manifestation.

B. burgdorferi is not known to produce toxins that damage host cells. Rather, clinical symptomatology is caused by the host inflammatory response (6). In some patients with Lyme arthritis, an exaggerated, dysregulated proinflammatory immune response develops, which can lead to persistent arthritis even after appropriate antibiotic therapy. This response is often referred to as postinfectious, antibiotic-refractory Lyme arthritis. The consequences in joint (synovial) tissues, which are the target of the immune response, include vascular damage, autoimmune and cytotoxic reactions, and massive fibroblast proliferation and fibrosis (7). What leads to the persistence of these symptoms is not well understood and likely involves multiple factors. We recently proposed peptidoglycan (PG) as one of these potential contributing factors (8). PG, an essential component of bacterial cell walls and a well-known immunogen (9), is made of glycan strands of repeating disaccharide-peptide units that form a crosslinked polymeric structure (known as a sacculus) around the bacterial cytoplasmic membrane. The *B. burgdorferi* PG (PG^{Bb}) has been demonstrated to be immunogenic, as purified PG^{Bb} sacculi induce an inflammatory response in mammalian cell cultures, C3H/HeJ mice, and humans (8, 10). Remarkably, evidence suggests that PG^{Bb} material can persist in the synovial fluids of Lyme arthritis patients, even months to a year after antibiotic treatment (8). Furthermore, these patients have a high level of anti-PG^{Bb} IgG antibodies detected within the synovial fluid of the affected joint (8). In the host, PG^{Bb} is detected by the innate immune receptor NOD2 (8). Interestingly, the transcript level of NOD2 transcripts is elevated in the inflamed synovial tissues of Lyme arthritis patients long after the resolution of the acute infection (11). In addition, mouse and in vitro cell experiments have linked NOD2 to proinflammatory cytokine production and immune tolerance during *B. burgdorferi* infection (12, 13). Altogether, these observations have led to the hypothesis that the persistence of residual PG^{Bb} contributes to the pathogenesis of Lyme arthritis (8) by acting as an adjuvant that stimulates chronic inflammation and/or by bolstering T cell proinflammatory immunoreactivity with autoantigens (14).

In live *B. burgdorferi* cells, the outer membrane shields the PG^{Bb} sacculus from immune detection by the host. However, two potential sources of PG^{Bb} exposure to the immune system have been proposed (8). First, when *B. burgdorferi* cells die due to the harsh conditions in the host (e.g., innate immunity or antibiotic treatment), they lyse, releasing PG^{Bb} material to the surrounding environment. Second, live spirochetes degrade ≈40% of their PG during growth but, unlike *Escherichia coli* and many other diderm bacteria (15), *B. burgdorferi* does not recycle PG turnover products during growth (8). As a result, growing *B. burgdorferi* cells continuously release PG^{Bb} fragments into the culture supernatant, possibly through diffusion across the outer membrane through porins.

These observations raise a number of questions. Do PG^{Bb} materials released from both dead and live spirochetes contribute to immunopathogenesis? Or is one source more likely to contribute than the other? If live *B. burgdorferi* does indeed release PG^{Bb} fragments into the environment during growth, how does this pathogen evade PG-based immune recognition and eradication by the host? Could the PG^{Bb} material shed from live *B. burgdorferi* cells be chemically distinct from the immunogenic PG^{Bb} of dead cells to avoid detection? Do PG hydrolases produced by *B. burgdorferi* and/or the host play a role in modulating immune response and pathogenesis? We sought to address these questions by characterizing the PG^{Bb} fragments released by live *B. burgdorferi* cells during growth and by identifying both bacterial and host factors that modulate PG^{Bb}-induced immune responses.

Results

Multiple *B. burgdorferi* strains shed peptidoglycan fragments of the same composition during growth. During growth, new disaccharide-peptides are incorporated into the existing PG sacculus. In *B. burgdorferi*, these PG precursors consist of *N*-acetyl-glucosamine (Glc*N*Ac) and *N*-acetyl-muramic acid (Mur*N*Ac) linked to a peptide chain made of L-alanine (L-Ala), D-glutamic acid (D-Glu), L-ornithine (L-Orn), and two D-alanine residues (D-Ala), with L-Orn being connected to a single glycine (Gly) (8, 10). The growing PG polymer is then crosslinked, remodeled, and trimmed by PG enzymes, leading to the mature sacculus illustrated in **Figure 1A** (8).

For this study, our first goal was to identify the major species of PG^{Bb} fragments that *B. burgdorferi* releases into its culture medium during growth. This was a nontrivial task, as laboratory cultures of *B. burgdorferi* require the use of a highly complex, undefined medium (e.g., BSK-II, which includes Glc*N*Ac, glucose, CMRL medium, bovine serum albumin, rabbit serum, neopeptone, and yeastolate). To find rare PG^{Bb} fragments in a complex mixture of other molecules in BSK-II, we developed a pipeline in which mass features enriched in the culture supernatant over the cell-free growth medium are screened against a library of simulated PG^{Bb} fragment masses (**Figure 1B**, see Materials and Methods). Briefly, replicates of a clonal derivative of the *B. burgdorferi* type strain B31 (B31 IR) were grown in BSK-II to late exponential phase (i.e., density of $\approx 5 * 10^7$ cells/mL). Culture supernatants ('Sup') were then harvested and analyzed by liquid chromatography (LC) coupled to mass spectrometry (MS) in comparison to the cell-free medium-only control ('BSK').

We found that over 2000 mass features displayed a significant ($p < 0.01$, Welch t-test and FDR-corrected) difference abundance (at least three-fold) between culture supernatants and the BSK-II control (**Figure 1C**). Most of these mass features were underrepresented in the cul-

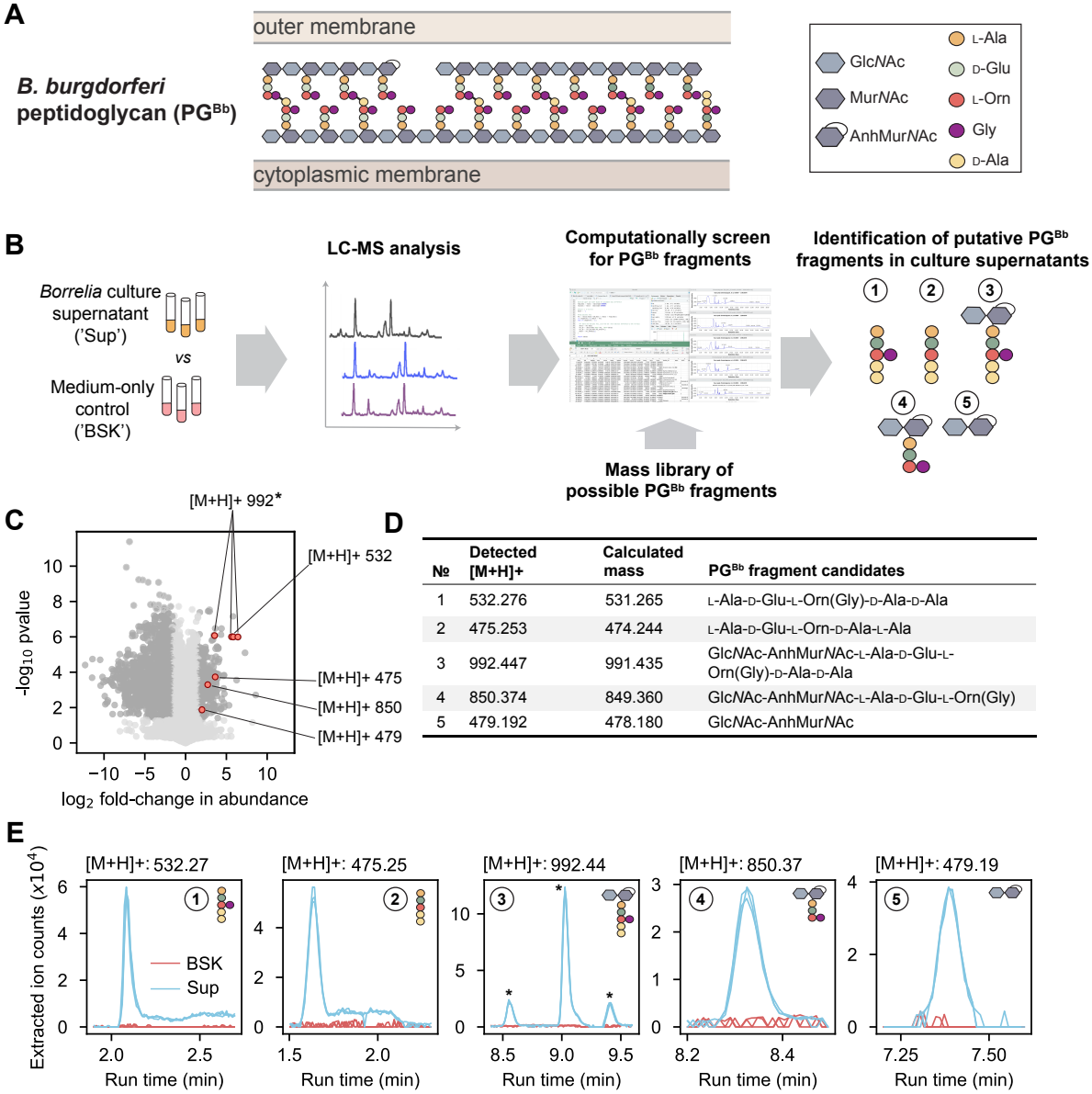

№	Detected [M+H]+	Calculated mass	PGBb fragment candidates
1	532.276	531.265	L-Ala-D-Glu-L-Orn(Gly)-D-Ala-D-Ala
2	475.253	474.244	L-Ala-D-Glu-L-Orn-D-Ala-L-Ala
3	992.447	991.435	GlcNAc-AnhMurNAc-L-Ala-D-Glu-L-Orn(Gly)-D-Ala-D-Ala
4	850.374	849.360	GlcNAc-AnhMurNAc-L-Ala-D-Glu-L-Orn(Gly)
5	479.192	478.180	GlcNAc-AnhMurNAc

Fig. 1. Mass spectrometry of *B. burgdorferi* culture supernatant identifies five peptidoglycan monomeric species. A. Schematic showing the chemical composition of the *B. burgdorferi* peptidoglycan (PG^{Bb}) and its location between the cytoplasmic and outer membranes. **B.** Workflow of the experimental approach: the supernatants ('Sup') of *B. burgdorferi* cultures vs. medium-only controls ('BSK') were analyzed by LC-MS to identify enriched mass features. Any enriched hits were compared against a mass library of potential PG^{Bb} monomers and dimers from which five candidate PG^{Bb} fragments were identified. **C.** Volcano plot of [M+H] features either enriched or depleted compared to medium only. Dark gray dots are mass features that are below the false discovery rate threshold of $p < 0.05$ and are greater than a fold-change of 3. Mass features that correspond to five candidate PG^{Bb} fragment candidates are indicated in red and labeled with the corresponding [M+H]+ values. The asterisk marks the PG^{Bb} fragment candidate with the same [M+H]+ value (992), but with three differently enriched isomers. The datapoint for one of these isomers overlaps with a datapoint for another putative PG^{Bb}fragment ([M+H]+ = 532). **D.** Table of predicted (calculated from our theoretical PG^{Bb} fragment library, **Supplementary Dataset 1**) and detected masses of the five candidate PG^{Bb}fragments identified in the culture supernatants. **E.** Individual extracted ion chromatograms (EICs) showing the enrichment of the PG^{Bb} fragment species in the supernatant (Sup) relative to medium-only control (BSK). The asterisks show the three peaks corresponding to isomeric forms of PG^{Bb} fragment #3.

ture supernatants, as expected from nutrients consumed from the BSK-II medium during *B. burgdorferi* growth. Of greater interest were the 270 mass features found to be enriched in the culture supernatants. To examine whether any of them might correspond to PG^{Bb} fragments, we computationally generated a mass library representing more than 700 permutations of possible PG^{Bb} monomers and dimers (**Supplementary dataset 1**, **Figure 1B**). Of the compounds that were undetectable in medium-only samples but present in culture supernatants, we found five molecules with masses corresponding to predicted monomeric PG^{Bb} species (**Figure 1D** and **Table S1**, PG fragment species #1-5). One of them ([M+H]+ = 992) was represented three times in **Figure 1C** due to the presence of isomers (marked by asterisks in **Figure 1E**). Two of the identified putative PG^{Bb} fragment candidates were peptide stem variants of the PG^{Bb}: one with Gly linked to Orn, L-Ala-D-Glu-L-Orn(Gly)-D-Ala-D-Ala (PG fragment #1), and the other without Gly, L-Ala-D-Glu-L-Orn-D-Ala-D-Ala (PG fragment #2). Two others were disaccharide-

peptides: Glc*N*Ac-AnhMur*N*Ac-L-Ala-D-Glu-L-Orn(Gly)-D-Ala-D-Ala (PG fragment #3) and Glc*N*Ac-AnhMur*N*Ac-L-Ala-D-Glu-L-Orn(Gly) (PG fragment #4). The remaining molecule consisted of the disaccharide moiety alone: Glc*N*Ac-AnhMur*N*Ac (PG fragment #5). All three sugar-containing candidates (PG fragments #3-5) were found to harbor Mur*N*Ac modified with an intramolecular 1,6-anhydro bond (Anh). This anhydro bond corresponds to the loss of a water molecule (18 Da). Plotting the extracted ion counts of the identified molecules demonstrated that all five PG fragment candidates were in quantities below the level of detection in the BSK II-only control, yet present in each of the three replicates culture supernatant samples analyzed (**Figure 1E**). The identity of each candidate was confirmed by tandem MS fragmentation (**Figures S1-S5**).

We found that these PG^{Bb} monomers accumulated during *B. burgdorferi* growth in BSK-II medium (**Figure 2A-B**), consistent with these molecules being the products of PG^{Bb} metabolism. This was observed not only for the strain B31 IR, our clonal derivative of the type strain B31 MI, but also for other *B. burgdorferi* strains, including K2, a clonal derivative of B31 MI amenable for cloning (16, 17), the infectious patient isolate strain 297 (18), and the infectious tick isolate N40 (19). We verified that B31 IR, K2, and N40 strains all have the expected complement of plasmids originally described for each strain (**Figure S6A-C**) (17, 20). Our strain 297 lacks cp32-6 and cp32-9 (**Figure S6D**) compared to the plasmid set previously described (20). We expect this strain to remain infectious as recent work has shown that cp32 plasmids are dispensable for infectivity in mice (21). A similar growth-dependent collection of PG^{Bb} fragments was found to accumulate in the culture medium of all four *B. burgdorferi* strains tested (**Figure 2B**).

BSK-II medium and one of its components, heat-inactivated rabbit serum, can possess residual peptidoglycan-hydrolytic activity. We noted that the levels of peptide- and disaccharide-only PG^{Bb} fragments continued to accumulate after the cultures reached stationary phase around day 7 (**Figure 2B**). In contrast, the levels of disaccharide-peptides often leveled off or decreased in these stationary phase cultures (**Figure 2B**). While these observations may reflect changes in PG enzymatic activities in stationary-phase *B. burgdorferi* cells, it also raised the possibility that the BSK-II medium itself may possess *N*-acetylmuramyl-L-alanine amidase activity that results in the cleavage of some shed disaccharide-peptides into their constituent parts (i.e., disaccharide- and peptide-only fragments). BSK-II growth medium contains rabbit serum at a final concentration of 6% (v/v), with standard heat inactivation of complement activity while preserving growth-promoting factors. Since rabbit serum has been reported to contain *N*-acetylmuramyl-L-alanine amidase activity (22), we reasoned that our heat-inactivated rabbit serum may still possess trace of amidase activity. If this were the case, incubation of purified PG^{Bb} sacculi in

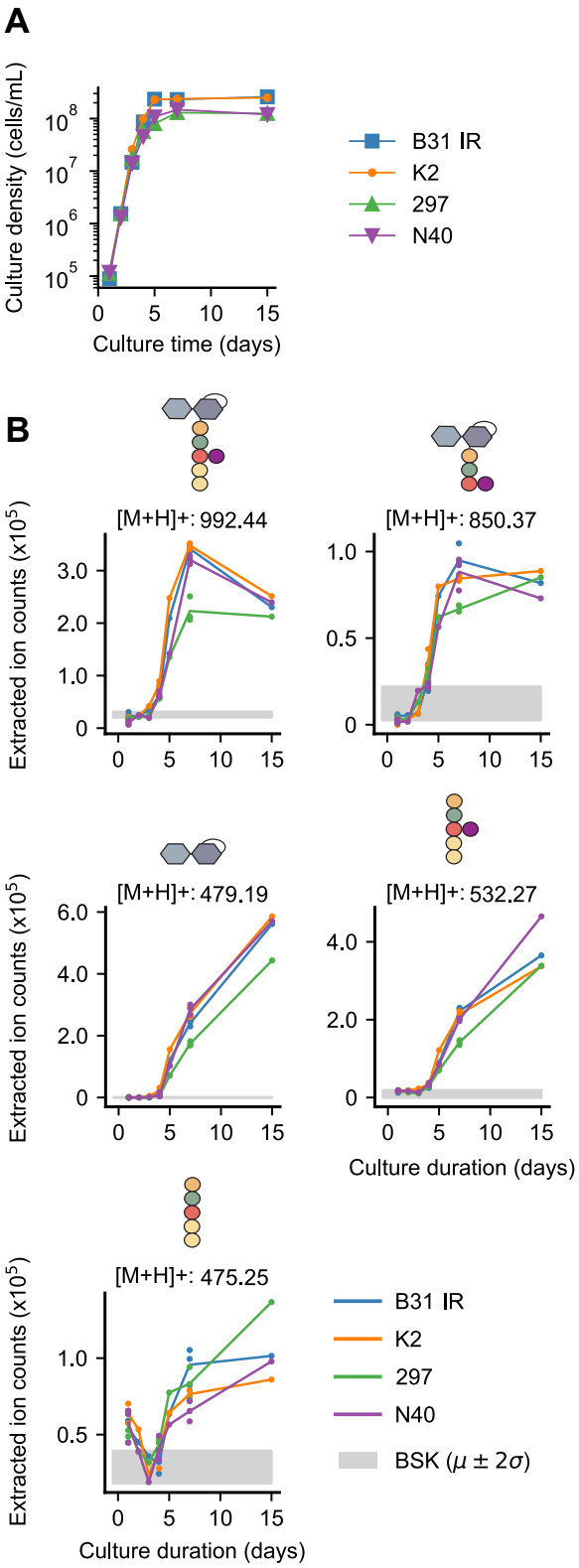

Fig. 2. Various *B. burgdorferi* strains accumulate PG^{Bb} monomers in their culture supernatants during growth. A. Growth curves of four indicated *B. burgdorferi* strains. **B.** Plots showing the accumulation (increase in extracted ion count) of the indicated PG^{Bb} fragment species in culture supernatants over time. Strains B31 IR, K2, 297, and N40 were sampled once daily during normal growth starting at a density of $1 * 10^4$ cells/mL. Three biological replicates are included for days 1, 4, and 7, while a single measurement was taken for days 2, 3, 5, and 15. The Grey shade shows the mean (μ) $\pm$ two standard deviations (2σ) for the background detection in the medium-only control (BSK).

complete BSK-II medium or in 100% heat-inactivated rabbit serum alone would be expected to result in the liberation of peptide-only PG fragments. Indeed, as shown by LC-MS analysis (**Figure S7**), we detected the accumulation of L-Ala-D-Glu-L-Orn(Gly) peptides, the prevalent peptide stem in the mature PG^{Bb} sacculus (**Figure 1A**) (8), in both BSK-II and heat-inactivated rabbit serum. These results suggest that at least a fraction of the disaccharide and peptide-only PG^{Bb} fragments found in the culture supernatant is generated by mammalian enzymes present in the BSK-II medium.

Peptidoglycan synthesis and turnover are largely coupled during *B. burgdorferi* growth. The prevalence of the peptide stem carrying a terminal D-Ala-D-Ala dimer among the PG^{Bb} fragments present in culture supernatants was surprising. D-Ala-D-Ala is predicted to be rare in the mature PG^{Bb} layer (**Figure 1A**) as it is not even detected in the chromatogram of muramidase-digested PG^{Bb} sacculi isolated from cells grown in vitro (8). Instead, unlinked peptide stems in the mature PG^{Bb} are almost exclusively of the form L-Ala-D-Glu-L-Orn(Gly) (**Figure 1A**). This suggests that the larger L-Ala-D-Glu-L-Orn(Gly)-D-Ala-D-Ala peptide stems present in PG^{Bb} precursor molecules are rapidly either crosslinked or trimmed by carboxypeptidases (CPases) to remove the terminal D-Ala residues and regulate the degree of crosslinking between glycan strands (23, 24). Accordingly, the PG^{Bb} sacculus of a *B. burgdorferi* mutant defective in CPase activity would be expected to contain a higher proportion of peptide stems with terminal D-Ala residues.

We obtained a *B. burgdorferi* mutant (strain T08TC493) with a Himar*1* transposon insertion at position 300 downstream of the first codon of the *bb0605* open reading frame, which is predicted to encode a CPase of 406 amino acids (25). We purified PG^{Bb} sacculi from *bb0605*::Himar*1* cells and compared their chemical composition to that of sacculi isolated from the B31-derived parent strain 5A18NP1 following enzymatic digestion of both sacculus preparations using mutanolysin, a muramidase that cleaves the β(1-4) glycosidic bond between Mur*N*Ac and Glc*N*Ac. The total-ion-count profiles representing digested sacculi from *bb0605*::Himar*1* and its parent differed considerably (**Figure 3A**). Note that each PG^{Bb} fragment typically eluted at more than one retention time, reflecting different isomeric forms. The extracted ion count profiles obtained for the parent strain revealed PG monomers primarily harboring peptide stems lacking D-Ala residues (variants i and ii in **Figure 3B**), consistent with the results of a previous PG^{Bb} digest analysis performed on another *B. burgdorferi* strain (8). In contrast, *bb0605*::Himar*1* sacculi demonstrated decreased abundance of such peptide stem variants (**Figure 3B**); instead, they were associated with a high proportion of PG monomers carrying longer peptide stems that contained D-Ala-D-Ala (variants iii and iv in **Figure 3C**). These data strongly suggest that BB0605 is an L,D-carboxypeptidase that prunes terminal D-Ala residues from PG^{Bb} peptide stems in wild-type cells. We propose this protein to be renamed D-Ala carboxypeptidase A (DacA) based on structural prediction comparison with an *E. coli* homolog of the same name (**Figure S8**) (26).

The LC-MS experiments with the *bb0605*::Himar*1* mutant also allowed us to determine the retention time of PG^{Bb} monomers harboring terminal D-Ala-D-Ala and verify that sacculi of the parent strain do indeed contain a small amount of these monomeric subunits (inset, **Figure 3C**). This small amount of D-Ala-D-Ala-containing peptide stems likely correspond to PG^{Bb} precursor molecules newly incorporated into the existing sacculus (i.e., before crosslinking and processing). This is consistent with our previous work showing that zones of new PG synthesis in *B. burgdorferi* are marked by fluorescent D-Ala analogs such as 7-hydroxycoumarincarbonylamino-D-alanine (HADA) upon their substitution for native D-Ala at the fifth amino acid position of the peptide stem (27). We reasoned that if the HADA signal previously observed in wild-type *B. burgdorferi* cells represents the low level of newly inserted D-Ala-D-Ala-containing peptide stems in the PG^{Bb} layer, this signal should increase considerably in the *bb0605*::Himar*1* mutant cells. As we reported previously (27), the addition of HADA to parent cell cultures for 1 h resulted in preferential accumulation of HADA signal at mid-cell due to enriched PG^{Bb} growth at that site, with occasional polar enrichment derived from division (**Figure 3D**). We observed the same overall spatial pattern of HADA labeling in *bb0605*::Himar*1* cells, but at a greater level, as shown qualitatively in images (**Figure 3E**) and by fluorescence signal quantification along the cell length (**Figure 3F**). This is consistent with an increased level of D-Ala-D-Ala-containing peptide stems in the PG^{Bb} layer in the absence of DacA activity. Increasing the time of HADA incorporation from 1 to 8 h (the latter approximating the generation time of *B. burgdorferi*) further increased the fluorescence signal intensity into the PG^{Bb} due to growth (**Figure 3D-F**). Altogether, our data suggest that, in a wild-type context, a considerable fraction of PG^{Bb} fragments shed into the environment is derived from D-Ala-D-Ala-containing PG^{Bb} material that had just been incorporated, before the D-Ala are removed by DacA or cross-linking. This indicates that the degradation of the PG is tightly coupled in time and space with its synthesis in *B. burgdorferi*.

BB0259 (MltS) contributes to the shedding of AnhMur*N*Ac-containing peptidoglycan monomers through lytic transglycosylase activity. Another characteristic of the released PG fragments we identified was that all three sugar-containing molecules contained AnhMur*N*Ac. No corresponding molecules containing Mur*N*Ac residues in hydrated/reducing form (i.e., no anhydro bond) were detected in culture supernatants (**Figure S9**). AnhMur*N*Ac-containing PG fragments are the product of bacterial enzymes known as lytic transglycosylases (LTGases) (28). These enzymes cleave the β(1,4)-

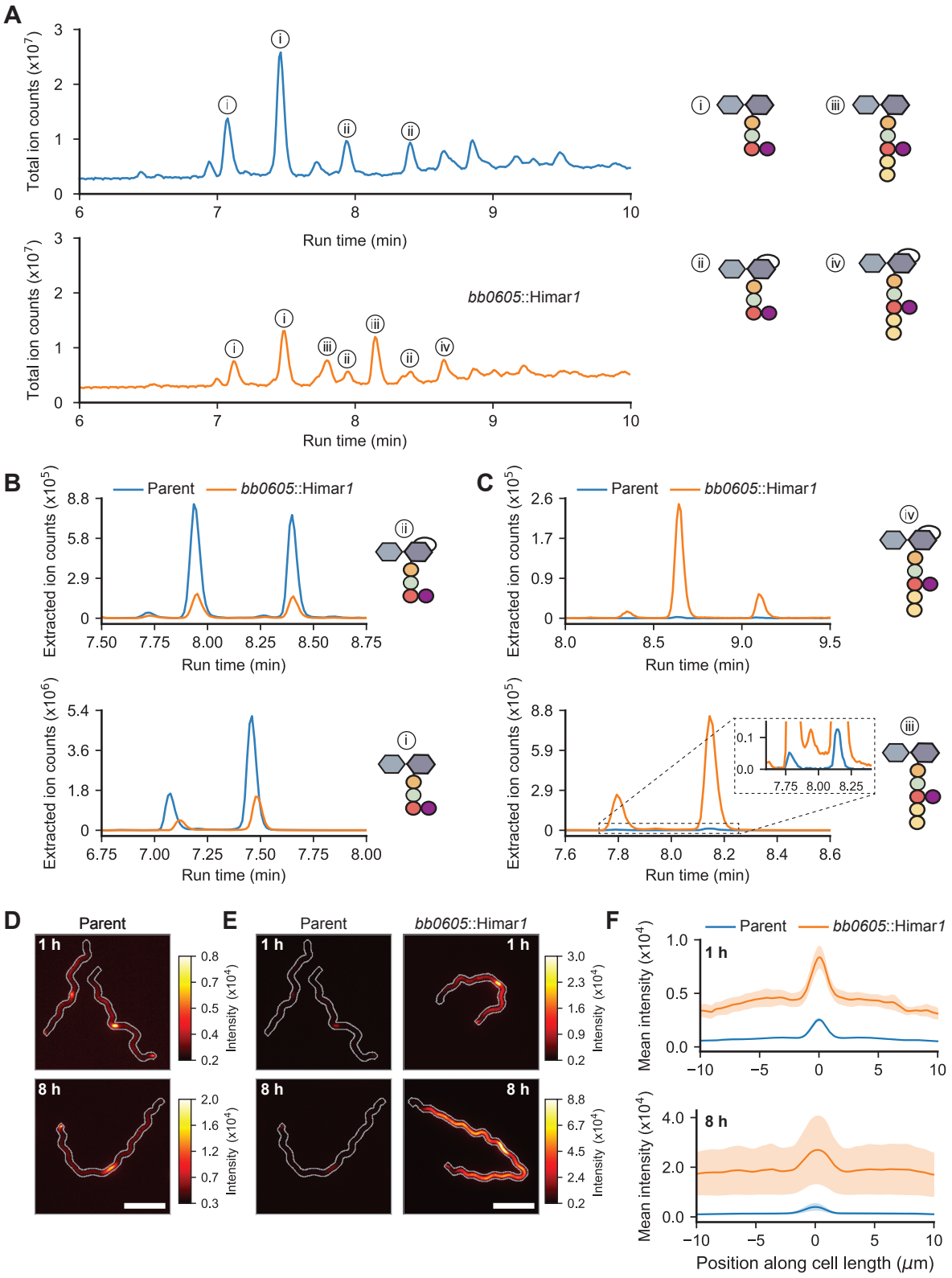

Fig. 3. BB0605 encodes an L,D-carboxypeptidase. A. Total ion chromatograms of parent (strain 5A18NP1) vs. *bb0605*::Himar*1* (strain T08TC493) sacculi digested with mutanolysin. Relevant peaks are denoted with numbers corresponding to the most abundant PG^{Bb} fragment species. **B.** Plots showing the extracted ion count (EIC) of Glc*N*Ac-AnhMur*N*Ac-L-Ala-D-Glu-L-Orn(Gly) (top) and Glc*N*Ac-Mur*N*Ac-L-Ala-D-Glu-L-Orn(Gly) (bottom) for the parent vs. *bb0605*::Himar*1* strains as a function of their run time through the liquid chromatography column. **C.** Same as (**B**) but for Glc*N*Ac-AnhMur*N*Ac-L-Ala-D-Glu-L-Orn(Gly)-D-Ala-D-Ala (top) and Glc*N*Ac-Mur*N*Ac-L-Ala-D-Glu-L-Orn(Gly)-D-Ala-D-Ala (bottom). **D.** Representative fluorescent images of parent cells stained with HADA for 1 and 8 h. Cell outlines were generated by making a mask of the cell in the corresponding phase contrast image, dilating it five times, and creating a contour of the binary mask. Scale bar is 5 μm. **E.** Same as (**D**) except that *bb0605*::Himar*1* cells are shown and that the HADA signal for parent cells are contrast-normalized to that of *bb0605*::Himar*1* cells. The look up table on the right applies to images with the same time point. **F.** Mean linescan intensities of HADA staining in parent vs. *bb0605*::Himar*1* cells. The shaded area represents the standard error of the mean (n = three biological replicates for each time point for which over 200 cells were analyzed per condition).

glycosidic linkage between Glc*N*Ac and Mur*N*Ac residues and, in the process, catalyze an intramolecular transglycosylation reaction that leads to the formation of an anhydro bond between C1 and C6 of Mur*N*Ac (28–31). When these enzymes act on the polymeric PG, the anhydro bonds they introduced into the PG sacculus prevent the incorporation of another disaccharide-peptide, thereby controlling the average length of glycan strands within the sacculus (28, 30, 32–34). Thus, AnhMur*N*Ac residues are found only at the end of glycan strands (**Figure 1A**) and are, as a consequence, found in low abundance in the PG layer relative to Mur*N*Ac residues. The activity of LTGases is also important for degrading large PG turnover products into small soluble fragments (35).

Based on sequence homology searches, *B. burgdorferi* has two putative LTGases (36). One of them, encoded by the *bb0259* gene, is required for the motility and wavy morphology of *B. burgdorferi* cells (36). This putative LTGase has been proposed to degrade PG^{Bb} above the site of flagellar basal body insertion into the cytoplasmic membrane to allow flagellar filament assembly across the PG^{Bb} layer (36). Based on gene deletion results, the other putative LTGase-encoding gene, *bb0531*, has no apparent effect on flagellar assembly, motility, or cell morphology (36). Since the LTGase activity had not previously been demonstrated for either gene product, we obtained *bb0259* and *bb0531* knockout strains (36) and examined their ability to release AnhMur*N*Ac-containing PG fragments into culture media relative to the parental strain. LC-MS revealed that the levels of all three AnhMur*N*Ac-containing PG turnover products present in the culture supernatants of the parent strain were considerably lower in the supernatants of the Δ*bb0259* cultures, but not in those of the Δ*bb0531* cultures (**Figure 4**). Furthermore, the levels of released AnhMur*N*Ac-containing molecules were largely restored in the Δ*bb0259* strain expressing wild-type *bb0259* from a shuttle vector (**Figure 4**), indicating phenotypic complementation. These results provide compelling evidence that *bb0259* encodes a bona fide LTGase that contributes to PG turnover and shedding in *B. burgdorferi*. Based on structural prediction, this *B. burgdorferi* LTGase shares similarity with the cytosolic *E. coli* Stl70 (**Figure S10**). However, BB0259 differs from Stl70 by being anchored to the inner membrane (37). Therefore, in consultation with Dr. Motaleb whose laboratory at East Carolina University generated the Δ*bb0259* strain used in this study (36), we propose the *bb0259* gene to be renamed *mltS* and its product, MltS, for "membrane-bound lytic transglycosylase in spirochetes."

The peptidoglycan monomers released during *B. burgdorferi* growth generate little to no NOD2-dependent inflammatory response in vitro. Our findings indicate that the PG^{Bb} fragments shed by live spirochetes during growth display chemical differences relative to the polymeric PG^{Bb} sacculus, which can become exposed when *B. burgdorferi* dies and lyses. How these chemical variations may affect the host immune response is not entirely clear. For instance, purified anhydromuramyl derivatives of Mur*N*Ac-peptides have been shown to be poor inducers of NOD2 (38, 39). On the other hand, the AnhMur*N*Ac-containing PG fragment Glc*N*Ac-AnhMur*N*Ac-L-Ala-D-Glu shed by *Neisseria* species has been described as a NOD2 agonist (40).

To examine this in the context of *B. burgdorferi* pathogenesis, we used a panel of synthetic PG^{Bb} fragments (30 μM) with varying chemical features (41). For simplicity, we will hereafter refer to PG fragments with both AnhMur*N*Ac and peptide moieties as anhydromuropeptides to distinguish them from the muropeptides that have reducing Mur*N*Ac residues. Our panel of synthetic molecules also included the well-known NOD2 agonist muramyl-dipeptide MDP (Mur*N*Ac-L-Ala-D-IsoGln) and its inactive isomer MDP-LL which serve as positive and negative controls, respectively (42, 43). For human cell immunostimulation, we first used human macrophage-like THP-1 cells differentiated using phorbol 12-myristate 13-acetate (PMA). These cells produce elevated levels of the cytokine interleukin-8 (IL-8) when stimulated with MDP (44), which we confirmed (**Figure 5A**). As expected, the negative control MDP-LL, had no stimulatory effect. All muropeptides (i.e., no anhydro bond) stimulated IL-8 production (**Figure 5A**). The presence of Glc*N*Acto form the disaccharide-peptide species did not stimulate IL-8 production to the same extent (**Figure 5A**). Importantly, all the corresponding anhydromuropeptides displayed little to no stimulatory activity of IL-8 production relative to their corresponding muropeptides ($p = 0.005$, **Figure S11A**). Peptide-only species also had no detectable stimulatory activity (**Figure 5A**). In a repeated comparative analysis, we included Glc*N*Ac-AnhMur*N*Ac-L-Ala-D-Glu-L-Orn(Gly)-D-Ala-D-Ala, the shed anhydromuropeptide with the two terminal D-Ala (PG^{Bb} fragment #3 in **Figure 1** and **Table S1**). This additional analysis confirmed that the presence of an anhydro bond considerably reduced the stimulation of IL-8 production irrespective of the presence or absence of the D-Ala-D-Ala moiety (**Figure S11B-C**).

To examine these effects in the context of NOD2, we tested the ability of key synthetic PG^{Bb} fragments to stimulate NF-κB in the HEK-Blue human NOD2 (hNOD2) reporter cell line relative to the NOD2-null parental cell line from which it was derived. For this experiment, we used two concentrations (1 and 30 μM) of synthetic PG^{Bb} fragments. The positive control (MDP) displayed strong NF-κB activation at both concentrations (**Figure 5B**), with a saturating absorbance (A_{655}) near 1.25 (**Figure S11D**). As expected, none of the peptides alone resulted in NF-κB activation whereas all tested muropeptides resulted in saturating NF-κB activation, even at the lowest concentration (**Figure 5B**). Conversely, exposure to the corresponding anhydromuropeptides resulted in little to no effect (**Figure 5B**). In all cases, the lowest concentration (1 μM) of a muropeptide generated a stronger response than the highest concentration (30 μM) of the corresponding anhydro-

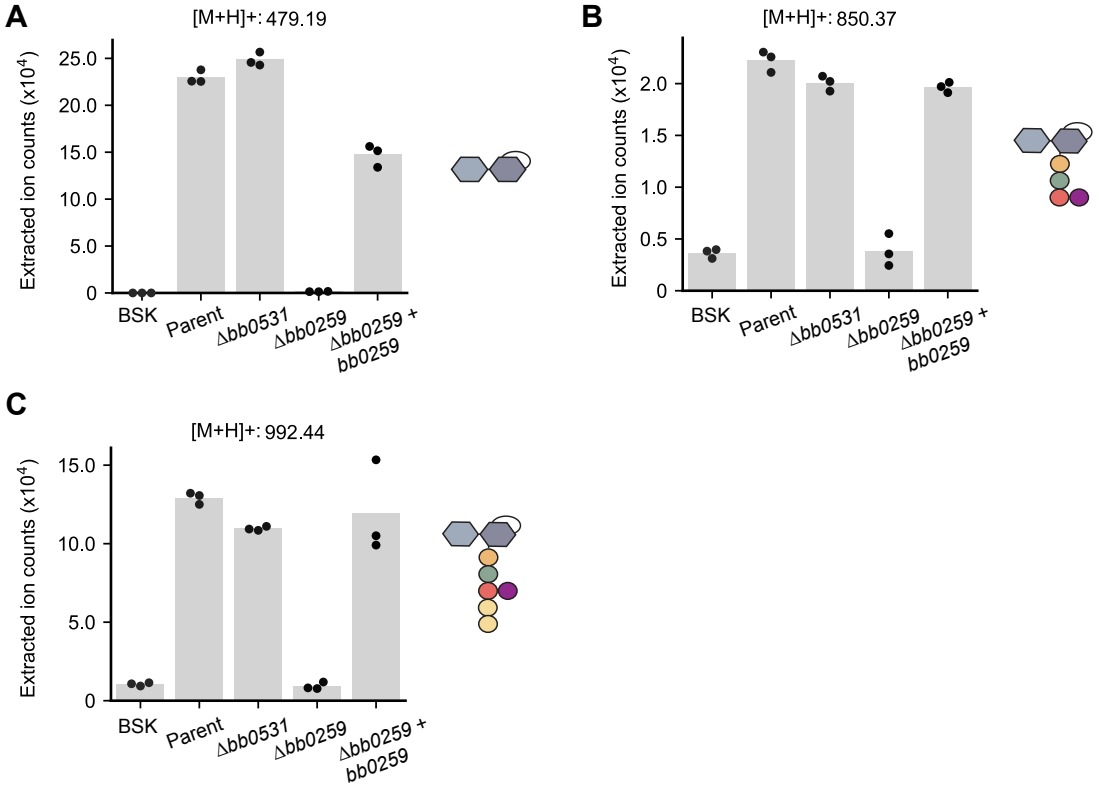

Fig. 4. The lytic transglycosylase BB0259 (renamed MltS) is responsible for the accumulation of AnhMur*N*Ac-containing PG^{Bb} species in culture supernatants. For all panels, the medium-only control (BSK) was compared to the culture supernatants of the following strains: parent (B31-A), Δ*bb0531*, Δ*bb0259* and Δ*bb0259* complemented by expression of *bb0259* from the *flgB* promoter on a shuttle vector (36). **A.** Plot showing the extracted ion counts (EIC) for Glc*N*Ac-AnhMur*N*Ac in the culture supernatants of the indicated strain. Dots represent data from three biological replicates, and the height of each bar represents the mean. Each EIC value was obtained by integrating the relevant peak for each PG^{Bb} fragment species. **B.** Same as (**A**) but for Glc*N*Ac-AnhMur*N*Ac-L-Ala-D-Glu-L-Orn(Gly) **C.** Same as (**A**) but for Glc*N*Ac-AnhMur*N*Ac-L-Ala-D-Glu-L-Orn(Gly)-D-Ala-D-Ala.

muropeptide, indicating that the anhydro bond formation on the Mur*N*Ac residue created by MltS decreases NOD2-dependent stimulation by at least 30-fold ($p = 0.04$, **Figure S12A**). Our results imply that through anhydro bond formation, the LTGase activity of MltS helps live *B. burgdorferi* evade NOD2-dependent detection despite continuously shedding PG^{Bb} material during growth.

The low immunogenicity of the shed PG^{Bb} monomers questioned the origin of the NOD2-stimulating NF-κB activity that our laboratory previously found in the supernatant of *B. burgdorferi* cultures (8). Therefore, we re-examined this activity on hNOD2 reporter cells and found no measurable stimulatory activity from culture supernatants of various *B. burgdorferi* strains compared to the positive control MDP (**Figure S12B**). The reason for the discrepancy is not clear. It is possible that the previously reported stimulatory activity originated from a gradual leakage of PG^{Bb} material from the sacculi of lysed or membrane-fragilized spirochetes into the culture over time. Leakage of PG material from dead cells may also explain residual NOD2-stimulatory activity previously reported for culture supernatants of *E. coli* and other bacterial species (45). We expect that PG contamination from dead cells may be more variable for *B. burgdorferi* cultures given that their "health" can easily fluctuate with small variations in the individual components of the complex growth medium, which can differ between batches (46–48). Furthermore, one of the essential components of the *B. burgdorferi* growth medium is serum, which contains innate immunity factors (e.g., complement system). If incompletely heat-inactivated, these factors may contribute to cell killing or membrane destabilization, which, in turn, could result in the release of immunogenic PG^{Bb} fragments into the culture. However, we cannot rule out the possibility that live *B. burgdorferi* cells do release immunostimulatory PG^{Bb} material below the detection level of our current MS and hNOD2 reporter assays. Regardless, such PG^{Bb} material would likely be a minor released product compared to the poorly immunogenic PG^{Bb} turnover products identified in this study. In contrast, the polymeric PG^{Bb} sacculus isolated from spirochetes after cell lysis is rich in the pro-inflammatory molecular motif Mur*N*Ac-L-Ala-D-Glu readily sensed by NOD2 relative to the corresponding anhydro-*N*-acetylmuramyl form (8). We found that pro-inflammatory Mur*N*Ac-peptide motifs remain abundant in PG^{Bb} sacculi isolated from 10-day-old stationary phase cultures (**Figure S13**) in which $> 90\%$ of the cells are dead (i.e., have lost their ability to proliferate upon nutrient repletion) (49). These results suggest that at least under these experimental conditions, the composition of the PG^{Bb} sacculus remains pro-inflammatory when *B. burgdorferi* dies.

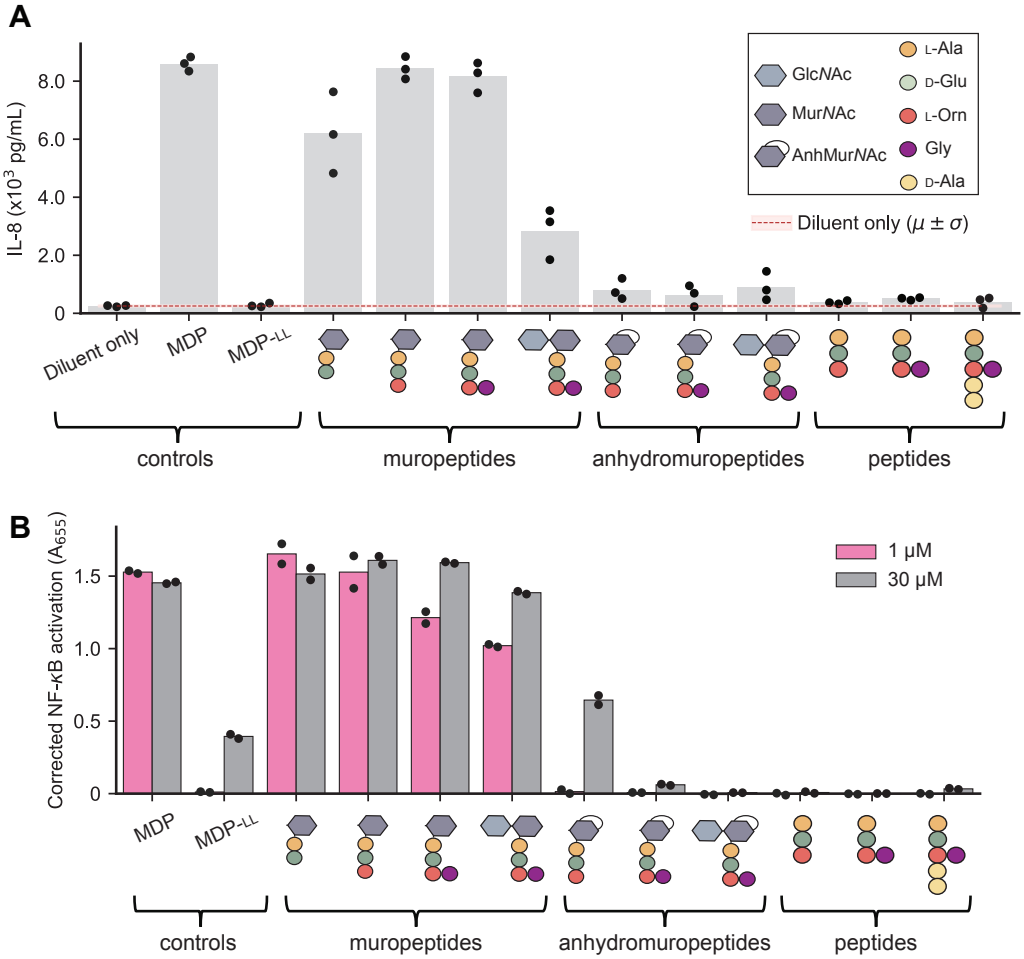

Fig. 5. The B. burgdorferi peptidoglycan-induced pro-inflammatory response is abrogated by the presence of AnhMur*N*Ac or the absence of a Mur*N*Ac residue. A. Plot showing IL-8 production in differentiated THP-1 cells in the presence of different synthetic PG fragments. Bar height represents the mean. Dots represent data from three biological replicates. The legend in the top right defines the schematics for the synthetic PG fragments. A statistical comparison between the muropeptides and the anhydromuropeptides is presented in **Figure S11A**. **B.** Plot showing secreted embryonic alkaline phosphatase (SEAP) activity, a proxy for NF-κB activation, measured as absorbance at 655 nm (A_{655}), in human NOD2 reporter cells (after correction using NOD2-null cells) following stimulation with the indicated molecules. Each dot represents a different biological replicate, and the bar height is the mean of the two replicates. A statistical comparison between the muropeptides and the anhydromuropeptides is presented in **Figure S12A**.

The levels of host peptidoglycan-hydrolytic activities vary between sera and synovial fluids across Lyme arthritis patients. The immunological results suggest that the primary immunostimulatory forms of PG^{Bb} derive from the sacculi, presumably when it becomes exposed after cell lysis. Exposed PG^{Bb} sacculi may then be digested by human hydrolytic enzymes. For instance, lysozyme has muramidase activity that cleaves the β(1,4)-glycosidic bond between Mur*N*Ac and Glc*N*Ac. But unlike MltS and other bacterial LTGases, lysozyme does not produce an anhydro bond on the Mur*N*Ac residues and instead releases muropeptides that are pro-inflammatory (as illustrated in **Figures 5**, **S11**, and **S12**). Humans can also produce an *N*-acetylmuramyl-L-alanine amidase, known as PGLYRP2 (50), which can abrogate PG^{Bb}-derived inflammatory activity by cleaving between Mur*N*Ac and L-Ala to release non-immunogenic peptides. Interestingly, human PG degrading activities can vary considerably across tissues and body fluids (51).

We reasoned that the levels of host PG hydrolytic activity could alter a PG^{Bb}-induced immune response depending on the anatomic sites that *B. burgdorferi* colonizes in patients. To examine this idea in the context of Lyme arthritis, we analyzed the digestion products of whole PG^{Bb} sacculi incubated for 0 or 6 h in either joint (synovial) fluid samples ($n = 6$) or serum ($n = 4$) from Lyme arthritis patients (color-coded in **Figure 6**) using LC-MS. The patients had a range of inflammatory responses and post-treatment durations of arthritis (see Materials and Methods for details). As an additional control, we analyzed the same set of 0 h incubation samples but without PG^{Bb} sacculi added. LC-MS analysis of the 6 h incubation products revealed predicted mass features of PG fragments in the bodily fluids that were virtually absent in the 0 h incubation samples or in the samples lacking PG^{Bb} sacculi (**Figures 6A** and **S14A**). This indicated that both fluids contained PG-hydrolytic activities. The release of disaccharides alone or in complex with a peptide indicated the presence of lysozyme activity in both fluids. However, the pattern of released fragments was distinct between sera and joint fluids. Incubation in joint

fluids produced largely saccharide-peptides and virtually no peptide- or saccharide-only fragments (**Figure 6A**). In contrast, incubation of *B. burgdorferi* PG sacculi in sera released not only various saccharide-peptide conjugates but also free saccharides and peptides (**Figure 6A**). The different enrichments of peptide-only masses in sera versus saccharide-peptide monomers in joint fluids are illustrated with a subset of PG fragments in **Figure 6B** (the complete set is shown in **Figure 6A**). The results indicate that while both types of fluid display muramidase activity (based on the presence of disaccharides alone or in complex with peptides), they considerably differ in their *N*-acetylmuramyl-L-alanine amidase activity. Serum samples had significant *N*-acetylmuramyl-L-alanine amidase activity that cleaved saccharide-peptides into individual saccharides and peptides, whereas joint fluid samples exhibited little, if any, such activity (**Figures 6A-B** and **S14B**). This was also true when comparing samples from the same (color-coded) patients. We also noted a wide variability in PG-hydrolytic activities across patients (**Figures 6A-B** and **S14**). The tissue-specific trends in PG-hydrolytic activities did not appear to be unique to Lyme arthritis patients as they could also be observed in the joint fluids of rheumatoid arthritis patients ($n = 3$) and the pooled serum of healthy individuals (**Figures 6** and **S14**).

To examine whether the observed differences in enzymatic activities could at least in part be attributed to differences in levels of lysozyme and PGLYRP2, we measured the abundance of these proteins in the same samples using an enzyme-linked immunosorbent assay (ELISA). This assay showed that the levels of lysozyme and PGLYRP2 in sera or joint fluids were indeed variable across individuals (**Figure 6C**). Samples with higher muramidase or *N*-acetylmuramyl-L-alanine amidase activity based on the overall PG^{Bb} digest profile (**Figure 6A**) had a higher concentration in lysozyme or PGLYRP2, respectively (**Figure 6C**). However, while the trends were preserved, the comparison was not fully consistent, suggesting that other unidentified PG-hydrolytic enzymes may be present in the samples. Importantly, the ELISA confirmed that joint fluids were associated with a generally lower level of PGLYRP2 compared to sera (**Figure 6**). Collectively, these findings suggest a potential role for human *N*-acetylmuramyl-L-alanine amidase activity in general and PGLYRP2 in particular in tissue-specific immunopathogenesis induced by lingering PG (as discussed below).

Discussion

Our study identifies the predominant PG fragments present in the supernatant of *B. burgdorferi* cultures (**Figure 1**). Our immunological assays (**Figures 5**, **S11**, and **S12**) suggest that these PG^{Bb} turnover products have low pro-inflammatory activity because of two key chemical features: (1) their peptide stems include an Orn residue at the third amino acid position (8, 10) in place of the more common DAP residue found in diderm bacteria (52), and (2) their Mur*N*Ac residues carry an anhydro bond linking C1 and C6. The presence of Orn instead of DAP precludes immune recognition by the PG-specific receptor NOD1 (53, 54) whereas the anhydro bond prevents detection by NOD2. Results from a recent study suggest a molecular mechanism for the latter effect, showing that NOD2 is preferentially activated by Mur*N*Ac-dipeptides that are phosphorylated by the mammalian *N*-acetylglucosamine kinase NAGK (55). Phosphorylation requires the availability of a hydroxyl group on the C6 position of Mur*N*Ac. The implication, which was not mentioned in the NAGK study (55), is that all anhydromuropeptides produced by bacterial LTGases (including MltS) cannot be phosphorylated by NAGK, as the process of anhydro bond formation eliminates the free hydroxyl group on C6 (29). Thus, in addition to limiting the length of glycan strands in the PG sacculus (28, 30, 32–34), LTGase activity also provides an effective means for bacteria to remodel their sacculi during growth without generating PG turnover products detectable by the NOD2 pathway. This conclusion is consistent with previous reports of the immunomodulatory effects of *Helicobacter pylori* and *Neisseria gonorrhoeae* LTGases (38, 39). Given the wide distribution of genes encoding LTGases across diverse bacterial phyla (29), the 1,6-anhydro linkages that these enzymes create in PG turnover products may represent an ancient strategy for evasion of NOD2-dependent immune response. This could particularly be a beneficial strategy for Gram-positive bacteria that most often produce Lys-type PG (52), which, like Orn-type PG, do not trigger a NOD1-dependent immune response (53, 54).

Whether the shed PG^{Bb} turnover products identified herein mediate beneficial interactions between *B. burgdorferi* and its various hosts in nature remains to be determined. Interestingly, anhydromuropeptides have been shown to act as chemical messengers between certain bacteria and their hosts, triggering cell signaling events unrelated to innate immune clearance (56–58). For example, anhydromuropeptide release has been shown to play a critical role in enabling the bacterium *Vibrio fischeri* to establish its symbiosis with the squid *Euprymna scolopes*. During growth, *V. fischeri* releases 1,6-anhydro-disaccharide-tetrapeptides that help trigger key morphogenic events in the squid's nascent light organ, ultimately facilitating its colonization by *V. fischeri* (59). By analogy, it is possible that 1,6-anhydro-disaccharide-peptides shed by *B. burgdorferi* during its growth in the midgut of a feeding tick may alter the tick vector's physiology to facilitate *B. burgdorferi* colonization or subsequent transmission. Further experimentation will be required to test this hypothesis. Using the *bb0259* knockout (ΔmltS) strain, which sheds little to no anhydromuropeptides (**Figure 4**), may seem attractive for such studies. However, the Δ*mltS* strain is already expected to be non-infectious due to its cell motility defect (36). It has been well-established that motility is critical for *B. burgdorferi*'s life cycle (60–62). It is also possible that the release of PG^{Bb} fragments during *B. burgdorferi* growth does not confer any fitness ad-

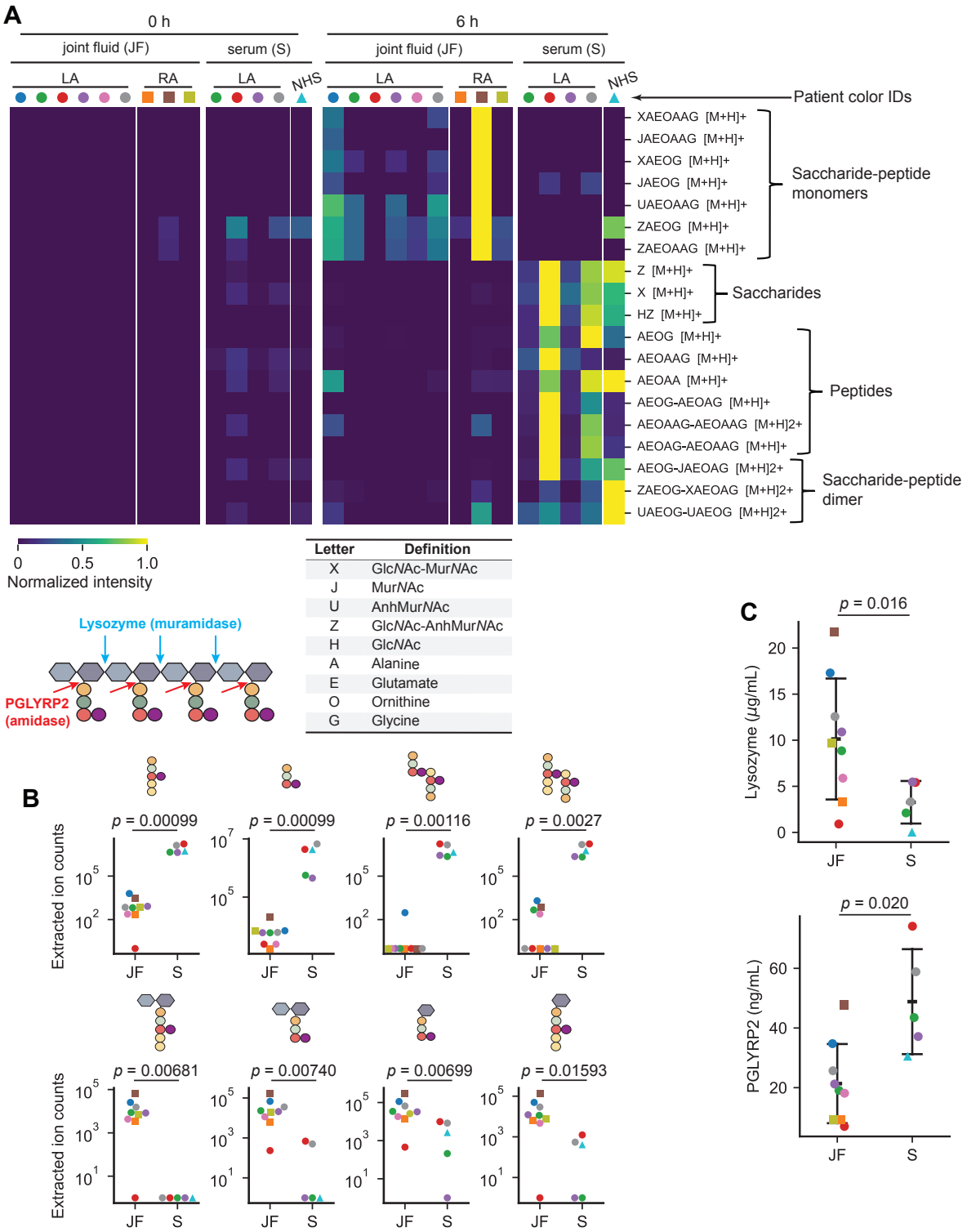

Letter	Definition
X	Glc*N*Ac-Mur*N*Ac
J	Mur*N*Ac
U	AnhMur*N*Ac
Z	Glc*N*Ac-AnhMur*N*Ac
H	Glc*N*Ac
A	Alanine
E	Glutamate
O	Ornithine
G	Glycine

Fig. 6. Incubation of *B. burgdorferi* sacculi in joint fluids and sera of Lyme arthritis patients causes the release of predicted PG^{Bb} fragments that vary in composition and amount. For all panels, the identities (IDs) of Lyme arthritis patients are color-coded. The same color indicates that the serum and joint fluid were obtained from the same individuals. **A.** Heatmap of predicted PG^{Bb} fragment species released from digestion of purified PG^{Bb} sacculi in six joint fluid samples and four serum samples from Lyme arthritis patients. For all samples, sacculi were incubated with either fluid for 0 h (left) or 6 h (right), then the resulting reaction products were analyzed by LC-MS. PG^{Bb} fragment species were detected by their predicted [M+H] value (**Table S1**, **Supplementary Dataset 1**). The accompanying table on the left contains the key to interpret the predicted identity of PG^{Bb} fragment species in the heatmap. Also shown is a schematic illustrating the cut sites for the indicated enzymes. **B.** Representative quantifications of peptide or sugar-peptide conjugate digestion products in serum and joint fluid samples predicted based on their masses. Each dot was derived from integrating the relevant EIC peak. Mann-Whitney U test was used to determine the p values as the data spanned log distances. **C.** ELISA results for either lysozyme or PGLYRP2 for the same joint fluid and serum samples as in (**A**) and (**B**). Error bars represent mean $\pm$ standard deviation. p values were obtained using a Welch t-test since the groups had unequal variances and N values.

vantage and is merely a consequence of the loss of PG recycling genes during the evolution of this spirochete as an obligate parasite, which has led to a reduction in genome size. *E. coli* mutants deficient for PG recycling have no reported fitness cost in laboratory cultures (58). Furthermore, while *B. burgdorferi* lacks the AmpG transporter [which is specific to PG fragments containing an anhydro-*N*-acetylmuramyl residue (63)], it carries other transporters that allows this pathogen to uptake precursors of PG synthesis (such as Glc*N*Ac and amino acids) from its host environment (64–66). This scavenging capability may obviate the need for a functional PG recycling pathway.

Importantly, our findings suggest that the pathogenic form of peptidoglycan in Lyme arthritis patients is polymeric PG^{Bb} material from dead spirochetes. In a study investigating *B. burgdorferi* burden and viability, all spirochetes identified in Lyme arthritis joint fluid samples were found to be moribund or dead, and spiking joint fluid samples (diluted $1:10$ or $1:100$) with 10^2, 10^4, or 10^6 cultured *B. burgdorferi* cells was found to result in rapid spirochete killing (67). Thus, the joint fluid, which contains high-titer *B. burgdorferi* antibodies, proinflammatory cytokines/chemokines, and complement components (68, 69), constitutes a generally lethal environment for spirochetes, thereby restricting infection to protected niches within the affected joint tissues (67). We hypothesize that immunogenic Mur*N*Ac-peptides from the PG^{Bb} sacculus become exposed to the immune system as *B. burgdorferi* cells lyse from the effects of initial immune responses or antibiotic treatment. Systemic injection of streptococcal PG in rats have shown that cell wall material can persist for weeks to months in the animals and that the localized presence of PG in joint tissues is associated with acute and chronic inflammation (70, 71). A study published during the revision of our manuscript demonstrates that polymeric PG^{Bb} persists in the joints of Lyme arthritis patients (72), consistent with PG^{Bb} from dead spirochetes being the pathogenic form.

In tissue culture of synovium from a patient with postinfectious Lyme arthritis, HLA-DR-expressing fibroblast-like synoviocytes, the most common cells in the synovial lesion, were found to be IFNγ-inducible antigen-presenting cells that present autoantigens (14). Moreover, when cultures were primed with IFNγ and PG^{Bb}, they secreted much higher levels of IFNγ, suggesting that the combination of IFNγ and PG^{Bb} may lead to enhanced activation of proinflammatory autoreactive T cells (14). Several host factors may bolster responsiveness to PG-derived immunogens. For instance, increased NOD2 expression has been identified in synovial tissues isolated from patients with postinfectious Lyme arthritis (11). In addition, the level of *N*-acetylmuramyl-L-alanine amidase activity and the abundance of PGLYRP2, which is expected to limit NOD2 activation, are low in synovial fluids—and thus presumably within the synovium—relative to serum (**Figures 6** and **S14**). Low PGLYRP2 activity, combined with elevated NOD2 level, may predispose joint tissues to PG^{Bb}-mediated inflammation. Furthermore, we observed a large variability in PGLYRP2 and other PG-hydrolytic activities across samples (**Figure 6**). Whether this variability contributes to differences in disease progression among individuals is an intriguing possibility that will require longitudinal studies to be examined. It is also worth noting that PGLYRP2 activity has been reported to be particularly low in cerebrospinal fluid (51), raising the possibility that PG^{Bb} may play a role in neuroborreliosis. Altogether, our study suggests a potential link between chronic inflammation and innate immunity.

Supplementing the inflamed tissues of Lyme arthritis patients with PGLYRP2 activity may, in theory, help mitigate PG-mediated immunopathology. Given the higher PGLYRP2 activity in the serum of Lyme arthritis patients (**Figure 6**), intraarticular injections of blood-derived products from autologous origin (i.e., obtained from the same individual) may be an effective treatment strategy for PG-induced pathology. For example, platelet-rich plasma injections are often used as orthobiologics to help heal damaged tissues (73, 74). Further studies on PGLYRP2 are recommended before exploring this treatment option for antibiotic-refractory Lyme arthritis and other potential PG-induced inflammatory pathologies (75–77), as PGLYRP2 may have pro-inflammatory activity downstream NOD2 (78).

Materials and Methods

Bacterial strains and growth conditions. Strains used in this study are detailed in **Table S2**. *B. burgdorferi* cells were cultured in complete Barbour-Stoenner-Kelly (BSK)-II medium in humidified incubators at 34℃ under 5% CO_2 atmosphere (64, 79, 80). Complete BSK-II contained 50 g/L bovine serum albumin (BSA, Millipore # 81-003), 9.7 g/L CMRL-1066 (US Biological # C5900-01), 5 g/L neopeptone (Thermo Fisher # 211681), 6 g/L HEPES acid (Millipore # 391338), 5 g/L D-glucose (Sigma # G7021), 2 g/L yeastolate (Difco # 255772), 0.7 g/L sodium citrate (Sigma # C7254), 0.8 g/L sodium pyruvate (Sigma # P5280), 2.2 g/L sodium bicarbonate (Sigma # S5761) and 0.4 g/L *N*-acetyl-glucosamine (Sigma # A3286). The pH of the medium was adjusted to 7.6, then supplemented with 60 mL/L heat-inactivated rabbit serum. Heat inactivation involved incubating the serum at 50℃ in a water bath for 30 min prior to use in medium preparation. Unless explicitly noted, all *B. burgdorferi* cultures were maintained in exponential phase at a density below $5*10^7$ cells/mL. Cell density was determined through direct cell counting using disposable Petroff-Hausser chambers and darkfield microscopy as previously described (81). When appropriate, relevant *B. burgdorferi* strains were cultured in the presence of antibiotics at the following final concentrations: 200 μg/mL for kanamycin (82) (Sigma # K1377), 40 μg/mL for gentamicin (83) (Sigma # G1914), and 100 μg/mL for streptomycin (16) (Sigma # S6501).

Verification of plasmid content in *B. burgdorferi* strains. Three biological replicates of *B. burgdorferi* strains B31 IR, K2, 297, and N40 were grown to a density between 1 and $4*10^7$ cells/mL in 14 mL complete BSK-II medium. The resulting cultures were centrifuged at 9000 x g for 5 min at 25℃. Cell pellets were processed using a QIAGEN DNeasy Blood & Tissue Kit (# 69504) to isolate genomic DNA (gDNA). Purified gDNA was sent for Illumina whole-genome sequencing using SeqCenter in Pittsburgh, PA, USA with a minimum read count of 1.33 million reads per sample. Different reference genomes were used for analysis: ASM4079079v1 for strain 297 (84, 85), ASM868v2 for strains B31 IR and K2 (85, 86), and ASM16663v1 for strain N40 (84, 85). Since the reference genome ASM4079079v1 for strain 297 is missing five cp32 plasmids, additional sequences were obtained from a previous study (20) and appended to the reference: cp32-1 (Accession # CP002254), cp32-5 (Accession # CP002261), cp32-6 (Accession # CP002263), cp32-9 (Accession # CP002262), and cp32-12 (Accession # CP002255). Reads were aligned to their respective reference using Breseq (87). The resulting alignment .bam files were then used to calculate coverage using the Python package `HTSeq` (88). The coverage array was loaded using the function `GenomicArray`, and then quantified using the function `GenomicInterval` for the number of reads in a 4000-bp search window across each genetic element. The counts in each search window were normalized to the total number of alignments for the genetic element in question. The fold change of each genetic element was calculated by taking the mean counts for each element and dividing it by the mean counts for the chromosome. Due to the repetitive nature of some *B. burgdorferi* plasmid sequences, plasmid elements with a fold change under the arbitrary value of 0.25 were counted as missing that plasmid.

Verification of the Himar*1* transposon insertion site in the *bb0605*::Himar*1* strain T08TC493. *B. burgdorferi* strains 5A18NP1 (B31-A) and T08TC493 (5A18NP1 *bb0605*::Himar*1*) were grown to $5*10^7$ cells/mL in 14 mL complete BSK-II. They were then centrifuged at 9000 x g for 5 min at 25℃. Cell pellets were then processed using a QIAGEN DNeasy Blood & Tissue Kit (# 69504) to isolate genomic DNA (gDNA). The *bb0605* locus was then amplified by PCR using primers 5'- `AAATGGCTCCTTTTTAATTGTATTGTAAT` -3' and 5'- `TTCACCAGGAACTATTATTGTAACAT` -3'. After confirming amplification by agarose gel electrophoresis, the remaining volume of PCR products was processed using a QIAquick PCR Purification Kit (QIAGEN # 28104) and then the PCR products were sequenced to determine the insertion site of the Himar*1* transposon, which was found to have disrupted the *bb0605* open reading frame 300 bp downstream of the first codon.

Purification of whole *B. burgdorferi* PG sacculi. Sacculi were purified in a manner similar to that described previously (89). Briefly, two flasks of 1 L BSK-II medium were inoculated with *B. burgdorferi* to a starting density of $1*10^4$ cells/mL. Once the cultures reached $1x10^8$ cells/mL (**Figures 3**, **6**, **S7**, and **S14**), or after 10 days in stationary phase (**Figure S13**), cells were centrifuged at 6000 x g for 20 min at 4℃ in successive 333 mL batches into the same two 500 ml polypropylene centrifuge tubes (Corning # 431123). Between each centrifugation, pellets were dislodged by vigorously swirling with the added culture. After the entire culture volume was centrifuged, the pellets were washed three times with cold phosphate-buffered saline (PBS, VWR # 76371-734), shaking vigorously to achieve a homogenous distribution of cells. The final pellets were stored at -80℃ overnight.

The following day, the pellets were resuspended in 6 mL chilled PBS and placed on ice. Separately, 6 mL of 10% w/v sodium dodecyl sulfate (SDS) per 1 L of cells to be processed was brought to a boil. The cell suspension in PBS was then added dropwise to the boiling SDS and allowed to continue boiling for an additional 30 min before being allowed to cool to room temperature. The lysed cell suspension was then transferred to glass culture tubes that were placed in a beaker filled appropriately with Milli-Q H2O. The glass culture tubes were mixed with a stir bar as the water was boiled for 2.5 h on a hotplate. The hotplate was subsequently turned off while the samples continued to be stirred overnight as they re-equilibrated to room temperature.

On the third day, the content of each tube was transferred to ultracentrifuge tubes and pelleted at 150,000 x g for 20 min at 20℃. The pellets were washed four times with 10.5 mL Milli-Q H_2O, centrifuging each time at 150,000 x g for 20 min at 20℃. After washing, the pellets were resuspended in 1 mL 100 mM Tris-HCl buffer (pH 7.5). Ten microliters of a 20 μg/mL solution of α-amylase (Sigma # 10102814001) were added to each suspension and incubated at 37℃ for 2 h, shaking at 220 rpm. Next, 1 mL Tris-HCl buffer (pH 7.5), 40 μL 1 M $MgSO_4$, and 2 μL nuclease mix [i.e., 100 μg/mL DNase I (Roche # 11284932001) + 500 μg/mL RNase A (Roche # 10109142001) dissolved in Milli-Q water] were added to each sample, followed by a 2 h incubation at 37℃ while shaking at 220 rpm. Lastly, 50μL of 50 mM $CaCl_2$ and 100 μL of a 2 mg/mL solution of chymotrypsin (Sigma # C4129) were added to each sample. The final suspensions were allowed to shake overnight at 220 rpm and 37℃.

On the final day, the chymotrypsin was inactivated by adding 200 μL of 10% SDS and boiling the samples in a water bath for 10 min. The contents of all tubes representing a common sample were combined into a single ultracentrifuge tube and washed six times with 10.5 mL Milli-Q H_2O. For each wash, the samples were centrifuged at 150,000 x g for 20 min at 20℃ in an ultracentrifuge. After the final wash, the pellet was resuspended in 1 mL sterile Milli-Q H_2O. Two hundred microliters of the final suspension were transferred to a pre-weighed Eppendorf tube for lyophilization. The dry mass of the lyophilized product was

measured to estimate the PG concentration of the starting suspension.

Extraction of PG^{Bb} fragments from culture supernatants. *B. burgdorferi* cultures at the relevant densities (between 10^4 and 10^8 cells/mL) were used (see **Figures 1**, **2**, **4**, **S1**-**S5**, **S7**, and **S9** for respective harvest times/cell densities). PG material was extracted using an acetonitrile:methanol extraction method. Briefly, 1 mL of relevant cultures was centrifuged and the supernatant filter-sterilized through a 0.1 μm PVDF syringe filter (Celltreat # 229740) into a separate tube, which was then stored at -20℃ until use. One hundred-fifty microliters of culture supernatant was mixed with 450 μL of a $1:1$ mixture of acetonitrile:methanol (prepared fresh, chilled to -20℃ before use), vortexed, and sonicated at room temperature for 10 min in a water bath sonicator. The sample was then placed at -20℃ for 1 h and vortexed every 30 min. Insoluble debris were pelleted at 15,000 x g for 20 min at 4℃, then ≈85% of the supernatant volume was carefully transferred to a new tube. The solution was dried in a Labconco centrivap (#7810014) at 37℃ for ≈6 h after which the pellets were stored at -20℃ until use. Samples were resuspended with 150 μL LC-MS grade water (MilliQ H_2O) for mass spectrometry.

Digestion of *B. burgdorferi* sacculi for liquid chromatography coupled to mass spectrometry. To determine the composition of PG^{Bb} sacculi isolated from either the *bb0605*::Himar*1* (T08TC493) strain or its parent (5A18NP1) (**Figure 3**), muramidase reactions were prepared consisting of 2 μL of mutanolysin (1 mg/mL), 2 μL of Tris-HCl (pH 7), ≈125 μg of PG, and Milli-Q H_2O to bring the final volume to 100 μL. These samples were vortexed, spun down, and then incubated overnight at 37℃, shaking at 700 rpm. The following day, digests were boiled at 100℃ for 5 min to denature the mutanolysin. The samples were then centrifuged at 20,000 x g for 15 min at room temperature. The supernatant was diluted $1:10$ in Milli-Q H_2O, with 150 μL being set aside for LC-MS. The same procedure was performed to analyze the composition of mutanolysin-digested PG^{Bb} sacculi isolated from 10-day-old stationary phase cultures of the B31 IR strain (**Figure S13**).

To assess the ability of joint fluids or sera from Lyme arthritis patients to digest PG, 5 μL whole sacculi (1.73 mg/mL) from strain T08TC493 was mixed with 90 μL of each body fluid and 5 μL Milli-Q H_2O. A negative control consisting only of 45 μL of each patient fluid and 5 μL Milli-Q H_2O was included. Half of the samples to which PG was added were immediately set aside to serve as a 0 h time point, while the rest of the samples was incubated at 37℃ for 6 h, shaking at 750 rpm. These samples were then stored at -20℃ until they were ready for processing. Once ready, 40 μL thawed samples were mixed with 160 μL $1:1$ mixture of acetonitrile:methanol. Following this, samples were processed further for LC-MS as described above.

To test whether components of the BSK-II medium degrade PG, 5 μL whole sacculi (1.25 mg/mL) purified from strain B31 IR was mixed with 5 μL Milli-Q H2O and 90 μL BSK-II medium (containing 6% of heat-inactivated rabbit serum) or 100% heat-inactivated serum. Replicates of rabbit serum were derived from separate lot numbers to check batch-to-batch variability. The "no PG^{Bb}" controls contained 45 μL of BSK II or heat-inactivated rabbit serum and 5 μL Milli-Q H_2O. Samples were incubated at 37℃ for 24 h, shaking at 750 rpm. Samples were then further processed for LC-MS as described above.

Liquid chromatography coupled to mass spectrometry. LC-MS experiments were performed using an Agilent QTOF 6545, coupled with an Agilent 1290 Infinity II ultra-high-pressure liquid chromatography (UHPLC) device. Samples were separated on a Kinetex Polar C18 column with a 100 Å pore size, 2.6 μm particle size and 2.1 x 100 mm in size (Phenomenex #00A-4759-AN), with the guard column Securityguard Ultra Holder (Phenomenex #AJ0-9000). Buffers used were A: LCMS-grade H_2O + 0.1% formic acid (Sigma # 1590132500) and B: acetonitrile + 0.1% formic acid (Sigma # 900686) on a gradient from 0–95% B. The gradient for the LC experiments is described in **Table S3**. The column temperature was maintained at 40℃ during the experiment. Ten microliters of sample were injected per run.

Quadrupole time-of-flight (QTOF) MS settings were as follows. All PG^{Bb} molecules were detected in the positive ionization mode with the instrument mass range set to 70-1700 Da. The scan rate was 1.5 spectra/s. Fragmentor voltage was set to 175 V. For MS/MS fragmentation (**Figures S1**-**S5**), the QTOF collision energy for the targeted released muropeptide masses was set as indicated in **Figures S1**-**S5**.

For analysis, Agilent ".d" files were converted into ".mzML" files using MSConvert (90). The python package `pymzmL` was used to analyze the mzML files (91). Extracted ion chromatograms were constructed using `pymzmL`'s run function and by searching each scan in the retention time for the candidate molecule ± 20 parts per million (ppm), while the total ion chromatograms summed total counts across every run time. Integrated signal for a single species was performed by summing the relevant area under the ion peaks.

The initial screen (**Figure 1C**) was analyzed using the XCMS package in R (92–94). Briefly, chromatogram peaks were detected using the function `findChromPeaks` with parameters defined by the function `CentWaveParam`. Peak criteria were defined as $ppm = 20$, $peakwidth = c(6, 30)$, $noise = 1000$, $prefilter = c(3, 1000)$, and $snthresh = 8$. Neighboring peaks were merged using the function `RefineChromPeaks`, specifying refining parameters with `MergeNeighboringPeaksParam`. Merging criteria were $expandRT = 0.1$, $ppm = 2.5$, and $minProp = 0.75$. Statistical significance was determined by XCMS's `pval` function, which uses a Welch's two-sample t-test. All signifi-

cant hits ($p < 0.05$, $fold\ change > 3$) were then checked against the theoretical PG^{Bb} masses in python using the packages `numpy` and `pandas` (95, 96). Identified targets were validated based on enrichment of EIC peaks in culture supernatants over BSK-II alone, valid isotopic distributions, and MS/MS fragmentation.

To screen for putative PG species (**Figures 6A** and **S14**), masses of theoretical PG^{Bb} fragment species were concatenated into a single vector containing all [M+H]+ and [M+H]2+ values. Extracted ion count (EIC) profiles were constructed for every value between retention times of 1 and 15 min of a 20-min run to exclude nonspecific compounds that wash off the column. `Scipy`'s `find_peaks` function was then used to identify peaks as $prominence = 1000$, $width = (6, 30)$ in retention time seconds, $rel_height = 1$ to capture width from the base of the peaks of interest, and $threshold = 7$ for a minimum signal-to-noise threshold. Identified hits were then verified to have an isotopic abundance distribution of two decaying peaks, the first of which being at least 1000 counts high. The most abundant peak was selected and summed for quantification. Identified masses from this process were then checked against the theoretical PG^{Bb} library. Identified hits were verified by constructing EICs profiles and checking that the elution profiles were consistent with previous observations. Inconsistent observations were removed from consideration.

Heat maps in **Figures 6A** and **S14** were compiled from the extracted ion counts, keeping only features that showed at least three-fold enrichment over the negative controls (0 h or no-PG^{Bb} conditions). The maximum value of extracted ions for features corresponding to identified PG^{Bb} species in any sample had to be at least $10,000$ to be considered.

Microscopy. The cell densities of *B. burgdorferi* cultures were determined by dilution in PBS and using an In-Cyto C-Chip disposable hematocytometer (InCyto # DHC-N01) and darkfield illumination in a Nikon Eclipse E600 microscope with a 40x 0.55 NA Ph2 phase contrast air objective and darkfield condenser lens. For fluorescence microscopy, samples were spotted on 2% PBS agarose pads (27, 97); covered with a No. 1.5 coverslip; and sealed with VALAP, a $1:1:1$ mixture of Vaseline petroleum jelly (Amazon ASIN B07MD6HJT4), lanolin (Spectrum # LA109) and paraffin wax (Fisher # 18-607-738), on all edges. Specimens were imaged using Nikon Eclipse Ti inverted microscopes with a 100x Plan Apo 1.45 NA phase contrast oil objective, Hamamatsu Orca-Flash4.0 V2 CMOS camera, a Sola LE light source (phase contrast), and a Spectra X Light engine. For the acquisition of fluorescent HADA images a DAPI filter set was used (Chroma 49028: ET395/25 ex, dichroic T425lpxr, ET460/50 em). The microscope was controlled by NIS-Elements AR.

HADA labeling of *B. burgdorferi* cells. Strains 5A18NP and T08TC493 were grown to high 10^6 or low 10^7 cells/mL densities. The morning of the experiment, 1 mL of each culture was set aside. Two microliters of 50 mM HADA (Tocris # 6647) were pipetted into each tube, which was then covered in aluminum foil and mixed by inversion. The samples were incubated at 34 ℃. After 1 h and 8 h of incubation, 200 μL was removed from the samples and placed in a 1.5 mL Eppendorf tube. These 200 μL aliquots were immediately centrifuged at 9,000 x g for 5 min at room temperature, washing two times in 500 μL BSK-II without phenol red. The final pellet was resuspended in 20-100 μL of phenol red-free BSK-II depending on the pellet size. Five microliters were spotted on a 2% PBS agarose pad for immediate imaging. Phase contrast images were acquired with a 500 ms exposure while HADA fluorescence was imaged with the DAPI filter set using 385 nm excitation at 40% power with an exposure of 1000 or 250 ms based on the 1 or 8 h of incubation time with HADA, respectively. For analysis, the intensity of cells was multiplied to equalize all time points to 1000 ms for comparison.

Image analysis. FIJI (98) was used for the preliminary assessment of fluorescence images, then Python was used for the remaining work. First, to facilitate analysis, we loaded large Nikon ND2 files as arrays using the previously published function `nd2_to_array` function (99). To create reliable masks of phase contrast images, an adaptive threshold from the Python package `OpenCV` (`cv2.adaptiveThreshold`) was applied, excluding objects smaller than 500 square pixels. Any surviving masks were kept and skeletonized. Cell skeletons were used to measure the width along the mask. Cells at least 4 μm long and cell masks less than 0.7 μm wide were selected. The surviving masks were assigned an ID and archived in a `Pandas` data frame for cell length and fluorescence measurements.

Linescans were generated by first measuring the medial axis down the center of the mask using the function `get_medial_axis` generated as before (100). The medial axis is a sub-pixel polynomial fitting from pole-to-pole. The medial axis was then used to measure cell lengths and retrieve the corresponding pixel intensities in the fluorescence image. The medial axis, cell length, and linescan measurements were also saved in the same Pandas data frame corresponding to each cell ID. Demographs were created by constructing a Python dictionary of all cell linescans in a dataset. They were ordered from shortest to longest, then arranged into a `numpy` array centered at midcell. Each line scan was normalized by z-score to show where signal was enriched.

To measure fluorescence in each cell, background-subtracted images were produced in Python using a modified background subtraction algorithm (99). Phase contrast images were segmented first using `OpenCV`'s adaptive threshold (`cv2.adaptiveThreshold`) to remove all potential fluorescing objects. These masks were dilated using `Scipy`'s `binary_dilation` function with ten iterations (101). The dilated objects were then removed from the fluorescent image. Surviving pixels were binned and

averaged using a rolling window across the x and y dimensions, then smoothed with a Gaussian kernel to obtain an estimated "background-only" image. Cell masks were used to measure the mean intensity (integrated intensity per unit pixel area) from every cell in the background-subtracted images.

Human subject samples. The study patients with Lyme arthritis met the criteria of the Centers for Disease Control and Prevention for *B. burgdorferi* infections (102). They had knee swelling and pain and positive antibody responses to *B. burgdorferi*, as determined by ELISA and Western blot. The patients were treated according to the guidelines of the Infectious Diseases Society of America (103). They had persistent arthritis despite one to two months of oral antibiotic therapy (usually doxycycline), followed by an additional one month of intravenous (IV) antibiotic therapy (ceftriaxone).

The six Lyme disease patients had a range of inflammatory responses and post-treatment durations of arthritis that were typical of more severe Lyme arthritis. Three patients had the resolution of arthritis one to three months after IV antibiotic therapy, whereas the other three had postinfectious arthritis lasting four to nine months after IV therapy. In three of the six patients, synovial fluid samples were obtained prior to starting IV antibiotic therapy when joints are typically swollen. In the remaining three patients, synovial fluid samples were obtained prior to starting synovectomy ($n = 1$) or therapy with disease-modifying antirheumatic drugs or DMARDs ($n = 2$). When samples were obtained, the median white cell count in synovial fluids was $17,022$ cells/mm3 (range $1,567$–$31,286$); whereas in blood, the median C-reactive protein (CRP) value was 28.4 (range 8–71.4), and the median erythrocyte sedimentation rate (ESR) was 28.5 (range 7–49). In four of the six patients, corresponding serum samples were available.

The three patients with rheumatoid arthritis had symmetrical polyarthritis affecting large and small joints. Samples were obtained during flares of arthritis one, four, and six years after disease onset. Patients were taking disease modifying anti-rheumatic drugs (DMARDs) at that time. Synovial fluid white cell counts ranged from $7,776$ to $20,300$ cells/mm^3, ESR values were high (62 to 66), and CRP values were also elevated (18.5 to 27.8). One patient had positive test results for both anti-citrullinated protein antibodies (ACPA) and rheumatoid factor (RF), one had a positive test for ACPA alone, and one had negative results for both tests.

To exclude sampling artifacts as an additional source of variation, serum and joint fluid samples were processed within hours after aspiration of synovial fluid. The samples were centrifuged at 300 x g for 10 min, followed by another centrifugation at 3000 x g for 10 min to remove cells and cell debris as previously described (104). Samples were stored in 1.5 mL aliquots in small plastic screw-top tubes and frozen at -80℃ without dilution or preservatives on the same day synovial fluid was obtained. Before each use, samples were centrifuged at 2,000 x g for 1 min to pellet potential remaining debris. No sample had undergone more than two freeze-thaw cycles before use in this study.

Enzyme-linked immunosorbent assays. Enzyme-linked immunosorbent assays (ELISA) were carried out using the PGLYRP2 ELISA Kit (MyBioSource # MBS2024542) and the Human Lysozyme ELISA Kit (Abcam # ab267798) using the manufacturer's protocol. The patient samples for PGLYRP2 detection were diluted 200-fold in PBS to fall within the dynamic range of the kit standards, while the samples for lysozyme detection were diluted 12,000-fold in PBS.

THP-1 and NOD2 reporter cell stimulation. The panel of synthetic PG^{Bb} molecules used for the immunological assays were synthesized as previously described (41). Two assays were performed to examine the immunostimulatory activities of these molecules. In the first one, THP-1 cells (ATCC # TIB-202) were grown in a humidified incubator at 37℃ under a 5% CO_2 atmosphere in complete RPMI (cRPMI) containing 10% fetal bovine serum (FBS) + 1% Pen-Strep (Gibco RPMI 1640 # 11875119; R&D systems FBS – premium select, heat inactivated # S11550H; Gibco Pen-Strep # 15140122), with cell densities maintained between $1 * 10^5$ and $1.5 * 10^6$ cells/mL. For PG^{Bb} stimulation experiments, THP-1 cells were differentiated into macrophage-like cells in the presence of phorbol 12-myristate 13-acetate (PMA, InvivoGen # tlrl-pma). More specifically, cells were diluted to $1.25 * 10^6$ cells/mL in cRPMI supplemented with 40 nM PMA, and 200 μL of the resulting cell suspension were added to the appropriate wells of a tissue culture-treated, flat-bottom 96-well plate (Fisher Scientific # FB012931) for a total of $2.5 * 10^5$ cells/well. After 48 h, the PMA-containing medium was removed by aspiration, 200 μL of fresh cRPMI lacking PMA was added to each well, and the cells were allowed to rest for 72 h. Following this rest period, the medium in each well was exchanged for serum-free RPMI and the cells were starved in this manner for 4 h prior to PG^{Bb} stimulation. At the end of this interval, the serum-free medium was removed from each well using an aspirating pipette and then replaced with cRPMI containing a synthetic PG^{Bb} fragment at a final concentration of 30 μM. To account for differences in stock concentrations, each of the different potential ligands tested was first diluted in ultrapure water (American Bio # AB02123) to a concentration of 1 mM prior to further dilution to 30 μM in cRPMI. After a 24-h stimulation period, the supernatant was harvested from each well and immediately frozen at -80℃. The supernatants were subsequently used for cytokine profiling by Luminex assay performed at Eve Technologies.

For the NOD2 reporter assay, HEK-Blue NOD2-overexpressing (hNOD2) and NOD2-deficient (Null2) cells (InvivoGen # hkb-hnod2v2 and hkb-null2, respectively) were maintained according to the manufacturer's rec-

ommendations. In brief, both cell lines were grown in Dulbecco's modified Eagle's medium (Sigma-Aldrich # D5796) containing 4.5 g/L glucose and 2 mM L-glutamine, and further supplemented with 10% FBS, 1% Pen-Strep, and 100 μg/mL Normocin (InvivoGen # ant-nr). Selective antibiotics were used in culturing both cell lines, beginning with the third passage after revival from frozen stock. Blasticidin (30 μg/mL, InvivoGen # ant-bl) and Zeocin (100 μg/mL, InvivoGen # ant-zn) were added to hNOD2 cell cultures, while only Zeocin was used for Null2 cell cultures. For PG^{Bb} stimulation and measurement of the resulting NOD2-dependent NF-κB activation by secreted embryonic alkaline phosphatase (SEAP) assay, 20 μL of each synthetic PG molecule was prepared by dilution in ultrapure water to a stock concentration of 300 μM and added to the appropriate wells of a tissue culture-treated, flat-bottom 96-well plate to the indicated final concentrations. The hNOD2 and Null2 cells were detached from the T75 flasks in which they had been expanded by exchanging the growth medium in each for 5 mL pre-warmed PBS and gently tapping the flask sides. Cells were fully resuspended by gentle pipetting and then counted using a disposable hemocytometer. Pre-warmed HEK-Blue Detection medium (InvivoGen # hb-det2; reconstituted according to manufacturer's recommendations) was then added to each cell suspension to achieve a final cell density of $2.8 * 10^5$ cells/mL. Next, 180 μL of the resulting cell suspension (or a total of approximately $5 * 10^4$ cells) were added to the appropriate wells of the 96-well plate described above such that the final PG fragment concentration in each well was either 1 or 30 μM. The plate was then placed at 37℃ in a humidified incubator containing 5% CO2 and SEAP production was assessed by absorbance measurement at 655 nm (Molecular devices, SpectraMax i3X) after 16 and 22 h of incubation.

For **Figure S11D**, about 50,000 HEK-Blue hNOD2 reporter cells (eighth passage) in a volume of 180 μL HEK-Blue Detection medium were added to each well containing 20 μL synthetic MDP (Invivogen # tlrl-mdp) diluted in ultrapure water such that the final MDP concentration ranged from 5 nM to 100 μM across a row of a 96-well plate. Plates were incubated for 16 h in a humidified incubator at 37℃ and 5% CO2, with subsequent absorbance measurements being obtained at 655 nm.

To prepare *B. burgdorferi* culture supernatants for HEK-Blue hNOD2 reporter stimulation (**Figure S12B**), *B. burgdorferi* starter cultures were used to inoculate 10 mL complete BSK-II medium (supplemented with 200 μg/mL kanamycin) to obtain a starting cell density of $\approx 10^4$ cells/mL. As a medium-only control, 10 mL complete BSK-II medium (also supplemented with kanamycin) was subjected to the same conditions (humidified 34℃ and 5% CO2 environment with tube cap loosened) as *B. burgdorferi* cultures. Once the cultures reached a spirochete density of $\approx 10^7$ cells/mL, cells were pelleted, and supernatants transferred to fresh tubes that were immediately stored at -80℃. Prior to application to HEK-Blue hNOD2-expressing reporter cells (fifth passage), thawed supernatants were passed through a 0.1 μm PES membrane filter (Foxx Life Sciences # 146-4113-RLS). HEK-Blue reporter cells were stimulated as before by exposure to 20 μL *B. burgdorferi* culture supernatant, complete BSK-II medium alone, MDP dissolved in ultrapure water (1 μM final concentration), or ultrapure water alone.

Computational analyses. For all custom-made analyses, R and Python scripts are available on the Jacobs-Wagner lab Github (https://github.com/JacobsWagnerLab/published/McCausland_et_al_2025). Python packages `numpy`, `scipy`, `scikit-image`, `seaborn`, and `pandas` used in this study have previously been described (95, 96, 101, 105, 106). The R package XCMS was previously described (94).

Data availability

Raw MS data are available in the GlycoPOST repository (107) under accession numbers GPST000537 and GPST000595. Raw microscopy images are available in the BioImage Archive (108) under the accession number S-BIAD1573. All other datasets and code for image and MS data analysis can be downloaded from the Jacobs-Wagner lab Github (https://github.com/JacobsWagnerLab/published/McCausland_et_al_2025).

ACKNOWLEDGEMENTS
We would like to thank Drs. Jonathon Z. Long, Veronica L. Li, Yuqin Dai, and Mengying Fu for their guidance on the mass spectrometry experiments. We also thank the Nucleus at the Stanford Sarafan ChEM-H insititute for access to mass spectrometry equipment. We are also grateful to the Jacobs-Wagner Laboratory for support, discussion, and critical reading of the manuscript. We would also like to thank the members of the Rego and Bockenstedt laboratories at Yale School of Medicine for providing lab space, equipment, and expertise to Z.A.K. to facilitate this work. This research was supported in part by funding from the James D. Jamieson and Family M.D.-Ph.D. Scholarship Fund at Yale University (to Z.A.K), the Medical Scientist Training Grant T32 GM007205 from the National Institute of General Medical Sciences, National Institutes of Health (to Z.A.K), the Stanford Bio-X Interdisciplinary Initiatives Seed Grants Program (IIP) [R10-9] (to C.J.-W.), the National Institutes of Health (R01GM138599 to C.L.G), and the Younger Family (to C.J.-W.). C.J.-W. is an investigator of the Howard Hughes Medical Institute. Portions of this work were originally part of the dissertation of one of the co-first authors (Z.A.K.). The funders had no role in study design, data collection and analysis, decision to publish, or preparation of the manuscript.

Author Contributions
Conceptualization: Irnov Irnov, Zachary A. Kloos, Christine Jacobs-Wagner
Data Curation: Joshua W. McCausland, Irnov Irnov
Formal Analysis: Joshua W. McCausland, Irnov Irnov
Funding Acquisition: Christine Jacobs-Wagner, Catherine L. Grimes
Investigation: Joshua W. McCausland, Zachary A. Kloos, Irnov Irnov, Nicole D. Sonnert, Junhui Zhou, Rachel Putnick, Elizabeth A. Mueller
Methodology: Irnov Irnov
Project Administration: Christine Jacobs-Wagner
Resources: Allen C. Steere, Catherine L. Grimes
Software: Joshua W. McCausland
Supervision: Christine Jacobs-Wagner, Catherine L. Grimes, Noah W. Palm
Validation: Joshua W. McCausland
Visualization: Joshua W. McCausland, Irnov Irnov
Writing – Original Draft and Preparation: Joshua W. McCausland, Christine Jacobs-Wagner
Writing – Review & Editing: Joshua W. McCausland, Zachary A. Kloos, Irnov Irnov, Nicole D. Sonnert, Junhui Zhou, Rachel Putnick, Elizabeth A. Mueller, Allen C. Steere, Catherine L. Grimes, Christine Jacobs-Wagner

Bibliography

1. Kugeler KJ, Earley A, Mead PS, Hinckley AF. Surveillance for lyme disease after implementation of a revised case definition - United States, 2022. Morbidity and Mortality Weekly Report. 2024;73(6):118–123.

2. Mead PS. Epidemiology of Lyme Disease. Infectious Disease Clinics of North America. 2015;29(2):187–219.
3. Mead PS, Schwartz A. In: Radolf JD, Samuels DS, editors. Epidemiology of Lyme Disease. Caister Academic Press; 2021.
4. Pustijanac E, Bursic M, Millotti G, Paliaga P, Ivesa N, Cvek M. Tick-born bacterial diseases in Europe: Threats to public health. European Journal of Clinical Microbiology & Infectious Diseases. 2024;43:1261–1295.
5. Radolf JD, Caimano MJ, Stevenson B, Hu LT. Of ticks, mice and men: Understanding the dual-host lifestyle of Lyme disease spirochaetes. Nature Reviews Microbiology. 2012;10(2):87–99.
6. Arvikar SL, Steere AC. Diagnosis and treatment of Lyme arthritis. Infectious Disease Clinics of North America. 2015;29(2):269–280.
7. Lochhead RB, Strle K, Arvikar SL, Weis JJ, Steere AC. Lyme arthritis: linking infection, inflammation, and autoimmunity. Nature Reviews Rheumatology. 2021;17:449–461.
8. Jutras BL, Lochhead RB, Kloos ZA, Biboy J, Strle K, Booth CJ, et al. *Borrelia burgdorferi* peptidoglycan is a persistent antigen in patients with Lyme arthritis. Proceedings of the National Academy of Sciences. 2019;116(27):13498–13507. doi:doi:10.1073/pnas.1904170116.
9. Wolf AJ, Underhill DM. Peptidoglycan recognition by the innate immune system. Nature Reviews Immunology. 2018;18(4):243–254.
10. Beck G, Benach JL, Habicht GS. Isolation, preliminary chemical characterization, and biological activity of Borrelia burgdorferi peptidoglycan. Biochemical and Biophysical Research Communications. 1990;167(1):89–95.
11. Lochhead RB, Ordoñez D, Arvikar SL, Aversa JM, Oh LS, Heyworth B, et al. Interferon-gamma production in Lyme arthritis synovial tissue promotes differentiation of fibroblast-like synoviocytes into immune effector cells. Cellular Microbiology. 2019;21(2):e12992.
12. Oosting M, Berende A, Sturm P, ter Hofstede HJM, de Jong DJ, Kanneganti TD, et al. Recognition of *Borrelia burgdorferi* by NOD2 Is Central for the Induction of an Inflammatory Reaction. The Journal of Infectious Diseases. 2010;201(12):1849–1858. doi:10.1086/652871.
13. Petnicki-Ocwieja T, DeFrancesco AS, Chung E, Darcy CT, Bronson RT, Kobayashi KS, et al. Nod2 Suppresses *Borrelia burgdorferi* Mediated Murine Lyme Arthritis and Carditis through the Induction of Tolerance. PLOS ONE. 2011;6(2):1–13. doi:10.1371/journal.pone.0017414.
14. Rouse JR, Danner R, Wahhab A, Pereckas M, Nguyen C, McClune ME, et al. HLA-DR-expressing fibroblast-like synoviocytes are inducible antigen presenting cells that present autoantigens in Lyme arthritis. ACR Open Rheumatology. 2024;6(10):678–689.
15. Park JT, Uehara T. How bacteria consume their own exoskeletons (turnover and recycling of cell wall peptidoglycan). Microbiology and Molecular Biology Reviews. 2008;72(2):211–227.
16. Frank KL, Bundle SF, Kresge ME, Eggers CH, Samuels DS. aadA confers streptomycin resistance in Borrelia burgdorferi. Journal of Bacteriology. 2003;185(22):6723–6727.
17. Rego ROM, Bestor A, Rosa PA. Defining the Plasmid-Borne Restriction-Modification Systems of the Lyme Disease Spirochete *Borrelia burgdorferi*. Journal of Bacteriology. 2011;193(5):1161–1171. doi:doi:10.1128/JB.01176-10.
18. Steere AC, Grodzicki RL, Kornblatt AN, Craft JE, Barbour AG, Burgdorfer W, et al. The Spirochetal Etiology of Lyme Disease. New England Journal of Medicine. 1983;308(13):733–740. doi:10.1056/nejm198303313081301.
19. Barthold SW, Moody KD, Terwilliger GA, Duray PH, Jacoby RO, Steere AC. Experimental Lyme Arthritis in Rats Infected with *Borrelia burgdorferi*. The Journal of Infectious Diseases. 1988;157(4):842–845. doi:10.1093/infdis/157.4.842.
20. Casjens SR, Mongodin EF, Qiu WG, Luft BJ, Schutzer SE, Gilcrease EB, et al. Genome Stability of Lyme Disease Spirochetes: Comparative Genomics of Borrelia burgdorferi Plasmids. PLOS ONE. 2012;7(3):e33280. doi:10.1371/journal.pone.0033280.
21. Hillman C, Theriault H, Dmitriev A, Hansra S, Rosa PA, Wachter J. *Borrelia burgdorferi* lacking all cp32 prophage plasmids retains full infectivity in mice. EMBO reports. 2025;26(8):1997–2012. doi:https://doi.org/10.1038/s44319-025-00378-9.
22. Valinger Z, Ladesic B, Tomasic J. Partial purification and characterization of N-acetylmuramyl-L-alanine amidase from human and mouse serum. Biochimica et Biophysica Acta. 1982;701(1):63–71.
23. de Pedro MA, Cava F. Structural constraints and dynamics of bacterial cell wall architecture. Frontiers in Microbiology. 2015;6:449.
24. Sauvage E, Kerff F, Terrak M, Ayala JA, Charlier P. The penicillin-binding proteins: structure and role in peptidogly can biosynthesis. FEMS Microbiology Reviews. 2008;32:234–258.
25. Lin T, Gao L, Zhang C, Odeh E, Jacobs MB, Coutte L, et al. Analysis of an Ordered, Comprehensive STM Mutant Library in Infectious *Borrelia burgdorferi*: Insights into the Genes Required for Mouse Infectivity. PLOS ONE. 2012;7(10):e47532. doi:10.1371/journal.pone.0047532.
26. Ghosh AS, Young KD. Sequences near the Active Site in Chimeric Penicillin Binding Proteins 5 and 6 Affect Uniform Morphology of *Escherichia coli*. Journal of Bacteriology. 2003;185(7):2178–2186. doi:10.1128/jb.185.7.2178-2186.2003.
27. Jutras BL, Scott M, Parry B, Biboy J, Gray J, Vollmer W, et al. Lyme disease and relapsing fever Borrelia elongate through zones of peptidoglycan synthesis that mark division sites of daughter cells. Proceedings of the National Academy of Sciences. 2016;113(33):9162–9170. doi:doi:10.1073/pnas.1610805113.
28. Höltje JV, Mirelman D, Sharon N, Schwarz U. Novel type of murein transglycosylase in *Escherichia coli*. Journal of Bacteriology. 1975;124(3):1067–1076.
29. Dik DA, Marous DR, Fisher JF, Mobashery S. Lytic transglycosylases: concinnity in concision of the bacterial cell wall. Critical Reviews in Biochemistry and Molecular Biology. 2017;52(5):503–542.
30. Kraft AR, Templin MF, Höltje JV. Membrane-bound lytic endotransglycosylase in *Escherichia coli*. Journal of Bacteriology. 1998;180(13):3441–3447.
31. Taylor A, Das BC, Heijenoort JV. Bacterial-cell-wall peptidoglycan fragments produced by phage λ or Vi II endolysin and containing 1,6-anhydro-N-acetylmuramic acid. European Journal of Biochemistry. 1975;53:47–54.
32. Bohrhunter JL, Rohs PDA, Torres G, Yunck R, Bernhardt TG. MltG activity antagonizes cell wall synthesis by both types of peptidoglycan polymerases in *Escherichia coli*. Molecular Microbiology. 2021;115(6):1170–1180.
33. Sassine J, Pazos M, Breukink E, Vollmer W. Lytic transglycosylase MltG cleaves in nascent peptidoglycan and produces short glycan strands. The Cell Surface. 2021;7(2021):100053.
34. Yunck R, Cho H, Bernhardt TG. Identification of MltG as a potential terminase for peptidoglycan polymerization in bacteria. Molecular Microbiology. 2016;99(4):700–718.
35. Weaver AI, Alvarez L, Rosch KM, Ahmed A, Wang GS, van Nieuwenhze MS, et al. Lytic transglycosylases mitigate periplasmic crowding by degrading soluble cell wall turnover products. eLife. 2022;11:e73178. doi:10.7554/eLife.73178.
36. Xu H, Hu B, Flesher DA, Liu J, Motaleb MA. BB0259 Encompasses a Peptidoglycan Lytic Enzyme Function for Proper Assembly of Periplasmic Flagella in *Borrelia burgdorferi*. Frontiers in Microbiology. 2021;12. doi:10.3389/fmicb.2021.692707.
37. Toledo A, Huang Z, Coleman JL, London E, Benach JL. Lipid rafts can form in the inner and outer membranes of *Borrelia burgdorferi* and have different properties and associated proteins. Molecular Microbiology. 2018;108(1):63–76.
38. Chaput C, Ecobichon C, Cayet N, Girardin SE, Werts C, Guadagnini S, et al. Role of AmiA in the morphological transition of *Helicobacter pylori* and in immune escape. 2006. 2006;2(9):e97.
39. Knilans KJ, Hackett KT, Anderson JE, Weng C, Dillard JP, Duncan JA. Neisseria gonorrhoeae lytic trnasglycosylases LtgA and LtgD reduce host innate immune signaling through TLR2 and NOD2. ACS Infectious Diseases. 2018;3:624–633.
40. Harris-Jones TN, Chan JM, Hackett KT, Weyand NJ, Schaub RE, Dillard JP. Peptidoglycan fragment release and NOD activation by commensal Neisseria species from humans and other animals. Infection and Immunity. 2024;92(5):e0000424.
41. Putnik R, Zhou J, Irnov I, Garner E, Liu M, Bersch KL, et al. Synthesis of a Borrelia-burgdorferi-derived muropeptide standard fragment library. Molecules. 2024;29(14):3297.
42. Inohara N, Ogura Y, Fontalba A, Gutierrez O, Pons F, Crespo J, et al. Host recognition of bacterial muramyl dipeptide mediated through NOD2. The Journal of Biological Chemistry. 2003;278(8):5509–5512.
43. Mo J, Boyle JP, Howard CB, Monie TP, Davis BK, Duncan JA. Pathogen sensing by nucleotide-binding oligomerization domain-containing protein 2 (NOD2) is mediated by direct binding to muramyl dipeptide and ATP. Journal of Biological Chemistry. 2012;287(27):23057–23067.
44. Jakopin Ž, Corsini E. THP-1 Cells and Pro-Inflammatory Cytokine Production: An In Vitro Tool for Functional Characterization of NOD1/NOD2 Antagonists. International Journal of Molecular Sciences. 2019;20(17). doi:10.3390/ijms20174265.
45. Hasegawa M, Yang K, Hashimoto M, Park JH, Kim YG, Fujimoto Y, et al. Differential Release and Distribution of Nod1 and Nod2 Immunostimulatory Molecules among Bacterial Species and Environments*. Journal of Biological Chemistry. 2006;281(39):29054–29063. doi:https://doi.org/10.1074/jbc.M602638200.
46. Callister SM, Case KL, Agger WA, Schell RF, Johnson RC, Ellingson JL. Effects of bovine serum albumin on the ability of Barbour-Stoenner-Kelly medium to detect Borrelia burgdorferi. Journal of Clinical Microbiology. 1990;28(2):363–365.
47. Wang G, Iyer R, Bittker S, Cooper D, Small J, Wormser GP, et al. Variations in Barbour-Stoenner-Kelly culture medium modulate infectivity and pathogenecity of *Borrelia burgdorferi* clinical isolates. Infection and Immunity. 2004;72(11):6702–6706.
48. Yang X, Popova TG, Goldberg MS, Norgard MV. Influence of cultivation media on genetic regulatory patterns in *Borrelia burgdorferi*. Infection and Immunity. 2001;69(6):4159–4163.
49. Zhang J, Takacs CN, McCausland JW, Mueller EA, Buron J, Thappeta Y, et al. *Borrelia burgdorferi* loses essential genetic elements and cell proliferative potential during stationary phase in culture but not in the tick vector. Journal of Bacteriology. 2025;207(3):e00457–24. doi:10.1128/jb.00457-24.
50. Dziarski R, Gupta D. Review: Mammalian peptidoglycan recognition proteins (PGRPs) in innate immunity. Innate Immunity. 2010;16(3):168–174.
51. Vanderwinkel E, Pauw Pd, Philipp D, Have JPT, Bainter K. The human and mammalian N-acetylmuramyl-L-alanine amidase: distribution, action on different bacterial peptidoglycans, and comparison with human lysozyme activities. Biochemical and molecular medicine. 1995;54:26–32.
52. Vollmer W, Blanot D, De Pedro MA. Peptidoglycan structure and architecture. FEMS Microbiology Reviews. 2008;32(2):149–167.
53. Chamaillard M, Hashimoto M, Horie Y, Masumoto J, Qiu S, Saab L, et al. An essential role for NOD1 in host recognition of bacterial peptidoglycan containing diaminopimelic acid. Nature Immunology. 2003;4(7):702–707.
54. Girardin SE, Travassos LH, Hervé M, Blanot D, Boneca IG, Philpott DJ, et al. Peptidoglycan molecular requirements allowing detection by Nod1 and Nod2. Journal of Biological Chemistry. 2003;278(43):41702–41708.
55. Stafford CA, Gassauer AM, de Oliveira Mann CC, Tanzer MC, Fessler E, Wefers B, et al. Phosphorylation of muramyl peptides by NAGK is required for NOD2 activation. Nature. 2022;609(7927):590–596. doi:10.1038/s41586-022-05125-x.
56. Dworkin J. The medium is the message: Interspecies and interkingdom signaling by peptidoglycan and related bacterial glycans. Annual Reviews in Microbiology. 2014;68:137–154.
57. Irazoki O, Hernandez SB, Cava F. Peptidoglycan muropeptides: Release, perception, and functions as signaling molecules. Frontiers in Microbiology. 2019;10:500.
58. Jacobs C, Huang LJ, Bartowsky E, Normark S, Park JT. Bacterial cell wall recycling provides cytosolic muropeptides as effectors for beta-lactamase induction. The EMBO Journal. 1994;13(19):4684–4694. doi:https://doi.org/10.1002/j.1460-2075.1994.tb06792.x.
59. Koropatnick TA, Engle JT, Apicella MA, Stabb EV, Goldman WE, McFall-Ngai MJ. Microbial factor-mediated development in a host-bacterial mutualism. Science. 2004;306(5699):1186–1188.
60. Li C, Xu H, Zhang K, Liang FT. Inactivation of a putative flagellar motor switch protein FliG1 prevents *Borrelia burgdorferi* from swimming in highly viscous media and blocks its infectivity. Molecular Microbiology. 2010;75(6):1563–1576. doi:https://doi.org/10.1111/j.1365-2958.2010.07078.x.
61. Sultan SZ, Manne A, Stewart PE, Bestor A, Rosa PA, Charon NW, et al. Motility Is

Crucial for the Infectious Life Cycle of *Borrelia burgdorferi*. Infection and Immunity. 2013;81(6):2012–2021. doi:10.1128/iai.01228-12.
62. Sultan SZ, Sekar P, Zhao X, Manne A, Liu J, Wooten RM, et al. Motor Rotation Is Essential for the Formation of the Periplasmic Flagellar Ribbon, Cellular Morphology, and *Borrelia burgdorferi* Persistence within *Ixodes scapularis* Tick and Murine Hosts. Infection and Immunity. 2015;83(5):1765–1777. doi:10.1128/iai.03097-14.
63. Cheng Q, Park JT. Substrate Specificity of the AmpG Permease Required for Recycling of Cell Wall Anhydro-Muropeptides. Journal of Bacteriology. 2002;184(23):6434–6436. doi:10.1128/jb.184.23.6434-6436.2002.
64. Barbour AG. Isolation and cultivation of Lyme disease spirochetes. Yale J Biol Med. 1984;57(4):521–5.
65. DeHart TG, Kushelman MR, Hildreth SB, Helm RF, Jutras BL. The unusual cell wall of the Lyme disease spirochaete *Borrelia burgdorferi* is shaped by a tick sugar. Nature Microbiology. 2021;6(12):1583–1592. doi:10.1038/s41564-021-01003-w.
66. Rhodes RG, Atoyan JA, Nelson DR. The chitobiose transporter, *chbC*, is required for chitin utilization in *Borrelia burgdorferi*. BMC Microbiology. 2010;10:21.
67. Li X, McHugh GA, Damle N, Sikand VK, Glickstein L, Steere AC. Burden and viability of *Borrelia burgdorferi* in skin and joints of patients with erythema migrans or lyme arthritis. Arthritis & Rheumatology. 2011;63(8):2238–2247.
68. Kannian P, McHugh G, Johnson BJB, Bacon RM, Glickstein LJ, Steere AC. Antibody responses to *Borrelia burgdorferi* in patients with antibiotic-refractory, antibiotic-responsive, or non-antibiotic-treated Lyme arthritis. Arthritis & Rheumatology. 2007;56(12):4216–4225.
69. Steere AC, Hardin JA, Ruddy S, Mummaw JG, Malawista SE. Correlation of serum and cryoglobulin IgM with activity, and serum IgG with remission. Arthritis & Rheumatology. 1979;22(5):471–483.
70. Cromartie WJ, Craddock JG, Schwab JH, Anderle SK, Yang CH. Arhritis in rats after systemic injection of streptococcal cells or cell walls. Journal of Experimental Medicine. 1977;146.
71. Dalldorf FG, Cromartie WJ, Anderle SK, Clark RL, Schwab JH. The relation of experimental arthritis to the distribution of streptococcal cell wall fragments. American Journal of Pathology. 1980;100(2):383–402.
72. McClune ME, Ebohon O, Dressler JM, Davis MM, Tupik JD, Lochhead RB, et al. The peptidoglycan of *Borrelia burgdorferi* can persist in discrete tissues and cause systemic responses consistent with chronic illness. Science Translational Medicine. 2025;17(795):eadr2955. doi:10.1126/scitranslmed.adr2955.
73. Beitzel K, Allen D, Apostolakos J, Russel RP, McCarthy MB, Gallo GJ, et al. US definitions, current use, and FDA stance on use of platelet-rich plasma in sports medicine. Journal of Knee Surgery. 2015;28(1):29–34.
74. Jeyaraman M, Jeyaraman N, Ramasubramanian S, Balaji S, Muthu S. Evidence-based orthobiolgic practice: Current evidence review and future directions. World Journal of Orthopedics. 2024;15(10):908–917.
75. Holub MN, Wahhab A, Rouse JR, Danner R, Hackner LG, Duris CB, et al. Peptidoglycan in osteroarthritis synovial tissue is associated with joint inflammation. Arthritis Research & Therapy. 2024;26(1):77.
76. Schrijver IA, Melief MJ, Markusse HM, Van Aelst I, Opdenakker G, Hazenberg MP, et al. Peptidoglycan from sterile human spleen induces T-cell proliferation and inflammatory mediators in rheumatoid arthritis patients and healthy subjects. Rheumatology. 2001;40(4):438–446.
77. Schrijver IA, Melief MJ, Tak PP, Hazenberg MP, Laman JD. Antigen-presenting cells containing bacterial peptidoglycan in synovial tissues of rheumatoid arthritis patients coexpress costimulatory molecules and cytokines. Athritis & Rheumatology. 2000;43(10):2160–2168.
78. Clowers JS, Allensworth JJ, Lee EJ, Rosenzweig HL. Investigation of the peptidoglycan sensing molecule, PGLYRP-2, in murine inflammatory uveitis. British Journal of Ophthalmology. 2013;97(4):504–510. doi:10.1136/bjophthalmol-2012-302650.
79. Jutras BL, Chenail AM, Stevenson B. Changes in bacterial growth rate govern expression of the *Borrelia burgdorferi* OspC and Erp infection-associated surface proteins. Journal of Bacteriology. 2013;195(4):757–764.
80. Zückert WR. Laboratory Maintenance of *Borrelia burgdorferi*. Current Protocols in Microbiology. 2007;4(1):12C.1.1–12C.1.10. doi:https://doi.org/10.1002/9780471729259.mc12c01s4.
81. Takacs CN, Kloos ZA, Scott M, Rosa PA, Jacobs-Wagner C. Fluorescent Proteins, Promoters, and Selectable Markers for Applications in the Lyme Disease Spirochete *Borrelia burgdorferi*. Applied and Environmental Microbiology. 2018;84(24):e01824–18. doi:doi:10.1128/AEM.01824-18.
82. Bono JL, Elias AF, Kupko III JJ, Stevenson B, Tilly K, Rosa P. Efficient targeted mutagenesis in *Borrelia burgdorferi*. Journal of Bacteriology. 2000;182(9):2445–2452.
83. Elias AF, Bono JL, Kupko III JJ, Stewart PE, Krum JG, Rosa P. New antibiotic resistance cassettes suitable for genetic studies in Borrelia burgdorferi. Journal of Molecular Microbiology and Biotechnology. 2003;6(1):29–40.
84. Schutzer SE, Fraser-Liggett CM, Casjens SR, Qiu WG, Dunn JJ, Mongodin EF, et al. Whole-Genome Sequences of Thirteen Isolates of *Borrelia burgdorferi*. Journal of Bacteriology. 2011;193(4):1018–1020. doi:doi:10.1128/JB.01158-10.
85. Tatusova T, Ciufo S, Fedorov B, O'Neill K, Tolstoy I. RefSeq microbial genomes database: new representation and annotation strategy. Nucleic Acids Research. 2013;42(D1):D553–D559. doi:10.1093/nar/gkt1274.
86. Fraser CM, Casjens S, Huang WM, Sutton GG, Clayton R, Lathigra R, et al. Genomic sequence of a Lyme disease spirochaete, Borrelia burgdorferi. Nature. 1997;390(6660):580–586. doi:10.1038/37551.
87. Deatherage DE, Barrick JE. In: Sun L, Shou W, editors. Identification of Mutations in Laboratory-Evolved Microbes from Next-Generation Sequencing Data Using breseq. New York, NY: Springer New York; 2014. p. 165–188. Available from: https://doi.org/10.1007/978-1-4939-0554-6_12.
88. Putri GH, Anders S, Pyl PT, Pimanda JE, Zanini F. Analysing high-throughput sequencing data in Python with HTSeq 2.0. Bioinformatics. 2022;38(10):2943–2945. doi:10.1093/bioinformatics/btac166.
89. Alvarez L, Hernandez SB, de Pedro MA, Cava F. Ultra-sensitive, high-resolution liquid chromatography methods for the high-throughput quantitative analysis of bacterial cell wall chemistry and structure. Methods in Molecular Biology. 2016;1440:11–27.
90. Chambers MC, Maclean B, Burke R, Amodei D, Ruderman DL, Neumann S, et al. A cross-platform toolkit for mass spectrometry and proteomics. Nature Biotechnology. 2012;30(10):918–920. doi:10.1038/nbt.2377.
91. Bald T, Barth J, Niehues A, Specht M, Hippler M, Fufezan C. pymzML—Python module for high-throughput bioinformatics on mass spectrometry data. Bioinformatics. 2012;28(7):1052–1053. doi:10.1093/bioinformatics/bts066.
92. Gatto L, Gibb S, Rainer J. MSnbase, efficient and elegant R-based processing and visualization of raw mass spectrometry data. Journal of Proteome Research. 2021;20(1):1063–1069.
93. Rainer J, Vicini A, Salzer L, Stanstrup J, Badia JM, Neumann S, et al. A modular and expandable ecosystem for metabolomics data annotation in R. Metabolites. 2022;12(2):173.
94. Smith CA, Want EJ, O'Maille G, Abagyan R, Siuzdak G. XCMS: processing mass spectrometry data for metabolite profiling using nonlinear peak alignment, matching, and identification. Analytical Chemistry. 2006;78(3):779–787.
95. Harris CR, Millman KJ, van der Walt SJ, Gommers R, Virtanen P, Cournapeau D, et al. Array programming with NumPy. Nature. 2020;585(7825):357–362. doi:10.1038/s41586-020-2649-2.
96. McKinney W. pandas: a Foundational Python Library for Data Analysis and Statistics; 2011.Available from: https://api.semanticscholar.org/CorpusID:61539023.
97. Glaser P, Sharpe ME, Raether B, Perego M, Ohlsen K, Errington J. Dynamic, mitotic-like behavior of a bacterial protein required for accurate chromosome partitioning. Genes Development. 1997;11(9):1160–1168.
98. Schindelin J, Arganda-Carreras I, Frise E, Kaynig V, Longair M, Pietzsch T, et al. Fiji: an open-source platform for biological-image analysis. Nature Methods. 2012;9(7):676–682. doi:10.1038/nmeth.2019.
99. Mäkelä J, Papagiannakis A, Lin WH, Lanz MC, Glenn S, Swaffer M, et al. Genome concentration limits cell growth and modulates proteome composition in *Escherichia coli*. eLife. 2024;13:RP97465. doi:https://elifesciences.org/reviewed-preprints/97465.
100. Papagiannakis A, Yu Q, Govers SK, Lin WH, Wingreen NS, Jacobs-Wagner C. DNA/polysome phase separation and cell width confinement couple nucleoid segregation to cell growth in *Escherichia coli*. bioRxiv. 2024;doi:10.1101/2024.10.08.617237.
101. Virtanen P, Gommers R, Oliphant TE, Haberland M, Reddy T, Cournapeau D, et al. SciPy 1.0: fundamental algorithms for scientific computing in Python. Nature Methods. 2020;17(3):261–272. doi:10.1038/s41592-019-0686-2.
102. Wharton M, Chorba TL, Vogt RL, Morse DL, Buehler JW. Case definitions for public health surveillance. MMWR Recommendations and Reports. 1990;39(RR-13):1–43.
103. Lantos PM, Rumbaugh J, Bockenstedt LK, Falck-Ytter YT, Aguero-Rosnfeld ME, Auwaerter PG, et al. Clinical practice guidelines by the Infectious Diseases Society of America, American Academy of Neurology, and American College of Rheumatology: 2020 Guidelines for the prevention diagnosis, and treatment of Lyme disease. Neurology. 2021;96(6):262–273.
104. Lochhead RB, Strle K, Kim ND, Kohler MJ, Arvikar SL, Aversa JM, et al. MicroRNA expression shows inflammatory dysregulation and tumor-like proliferative responses in joints of patients with postinfectious lyme disease. Arthritis & Rheumatology. 2017;69(5):1100–1110.
105. van der Walt S, Schönberger JL, Nunez-Iglesias J, Boulogne F, Warner JD, Yager N, et al. scikit-image: image processing in Python. PeerJ. 2014;2:e453. doi:10.7717/peerj.453.
106. Waskom ML. seaborn: statistical data visualization. The Journal of Open Source Software. 2021;6(60):3021.
107. Watanabe Y, Aoki-Kinoshita KF, Ishihama Y, Okuda S. GlycoPOST realizes FAIR principles for glycomics mass spectrometry data. Nucleic Acids Research. 2020;49(D1):D1523–D1528. doi:10.1093/nar/gkaa1012.
108. Hartley M, Kleywegt GJ, Patwardhan A, Sarkans U, Swedlow JR, Brazma A. The BioImage Archive – Building a Home for Life-Sciences Microscopy Data. Journal of Molecular Biology. 2022;434(11):167505. doi:https://doi.org/10.1016/j.jmb.2022.167505.
109. Kempen Mv, Sim SS, Tumescheit C, Mirdita M, Lee J, Gilchrist CLM, et al. Fast and accurate protein structure search with Foldseek. Nature Biotechnology. 2023;42:243–246.
110. Berman HM, Westbrook J, Feng Z, Gilliland G, Bhat TN, Weissig H, et al. The Protein Data Bank. Nucleic Acids Research. 2000;28(1):235–242.
111. Nicholas RA, Krings S, Tomberg J, Nicola G, Davies C. Crystal structure of wild-type penicillin-binding protein 5 from Escherichia coli: Implications for deacylation of the acyl-enzyme complex. Journal of Biological Chemistry. 2003;278(26):52826–52833.
112. Meng EC, Goddard TD, Pettersen EF, Couch GS, Pearson ZJ, Morris JH, et al. UCSF ChimeraX: Tools for structure building and analysis. Protein Science. 2023;32(11):e4792.
113. van Asselt EJ, Thunnissen AMWH, Dijkstra BW. High resolution crystal structures of the Escherichia coli lytic transglycosylase slt70 and its complex with a peptidoglycan fragment. Journal of Molecular Biology. 1999;291(4):877–898.
114. Elias AF, Stewart PE, Grimm D, Caimano MJ, Eggers CH, Tilly K, et al. Clonal Polymorphism of Borrelia burgdorferi Strain B31 MI: Implications for Mutagenesis in an Infectious Strain Background. Infection and Immunity. 2002;70(4):2139–2150. doi:doi:10.1128/IAI.70.4.2139-2150.2002.
115. Leong JM, de Vargas LM, Isberg RR. Binding of cultured mammalian cells to immobilized bacteria. Infection and Immunity. 1992;60(2):683–686.
116. Chan K, Alter L, Barthold SW, Parveen N. Disruption of bbe02 by insertion of a luciferase gene increases transformation efficiency of *Borrelia burgdorferi* and allows live imaging in lyme disease susceptible C3H mice. PLoS One. 2015;10(6):e0129532.
117. Kawabata H, Norris SJ, Watanabe H. BBE02 Disruption Mutants of Borrelia burgdorferi B31 Have a Highly Transformable, Infectious Phenotype. Infection and Immunity. 2004;72(12):7147–7154. doi:doi:10.1128/IAI.72.12.7147-7154.2004.
118. Takacs CN, Wachter J, Xiang Y, Ren Z, Karaboja X, Scott M, et al. Polyploidy, regular patterning of genome copies, and unusual control of DNA partitioning in the Lyme disease spirochete. Nature Communications. 2022;13(1):7173. doi:10.1038/s41467-022-34876-4.

Supplemental Materials: Bacterial and host enzymes modulate the inflammatory response produced by the peptidoglycan of the Lyme disease agent

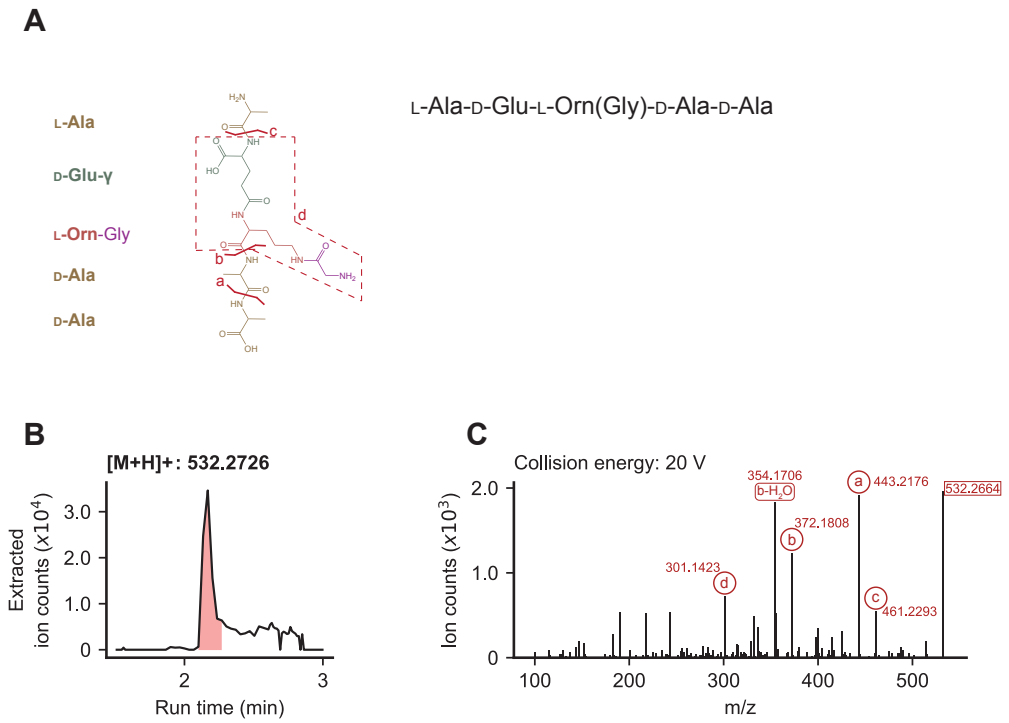

Fig. S1. Fragmentation of PG^{Bb} fragment L-Ala-D-Glu-L-Orn(Gly)-D-Ala-D-Ala. A. Schematic outlining each amino acid in L-Ala-D-Glu-L-Orn(Gly)-D-Ala-D-Ala, along with notations of the origin of each identified fragment after MS/MS. **B.** EIC profile of the identified [M+H]+ profile. The peak of interest is shaded in red. **C.** The MS2 spectrum at the run time where the EIC peak in (**B**) is at maximum intensity. The collision energy used to fragment this molecule is indicated, and each identified fragment is marked with a letter corresponding to the schematic in (**A**).

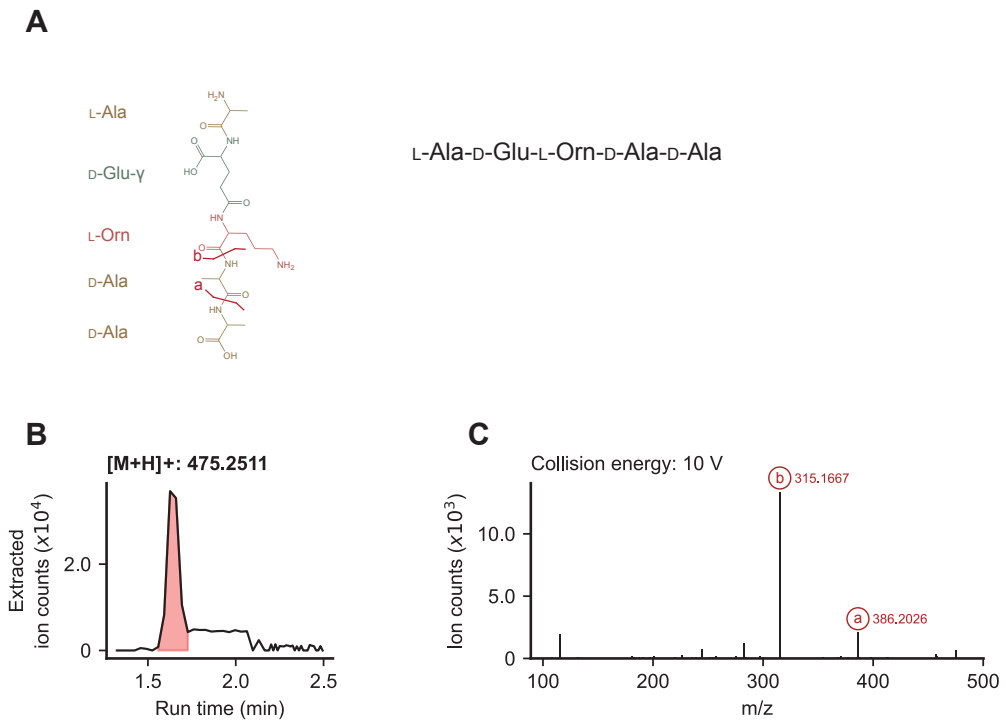

Fig. S2. Fragmentation of PG^{Bb} fragment L-Ala-D-Glu-L-Orn-D-Ala-D-Ala. A. Schematic outlining each amino acid in L-Ala-D-Glu-L-Orn-D-Ala-D-Ala, along with notations of the origin of each identified fragment after MS/MS. **B.** EIC profile of the identified [M+H]+ profile. The peak of interest is shaded in red. **C.** The MS2 spectrum at the run time where the EIC peak in (**B**) is at maximum intensity. The collision energy used to fragment this molecule is indicated, and each identified fragment is marked with a letter corresponding to the schematic in (**A**).

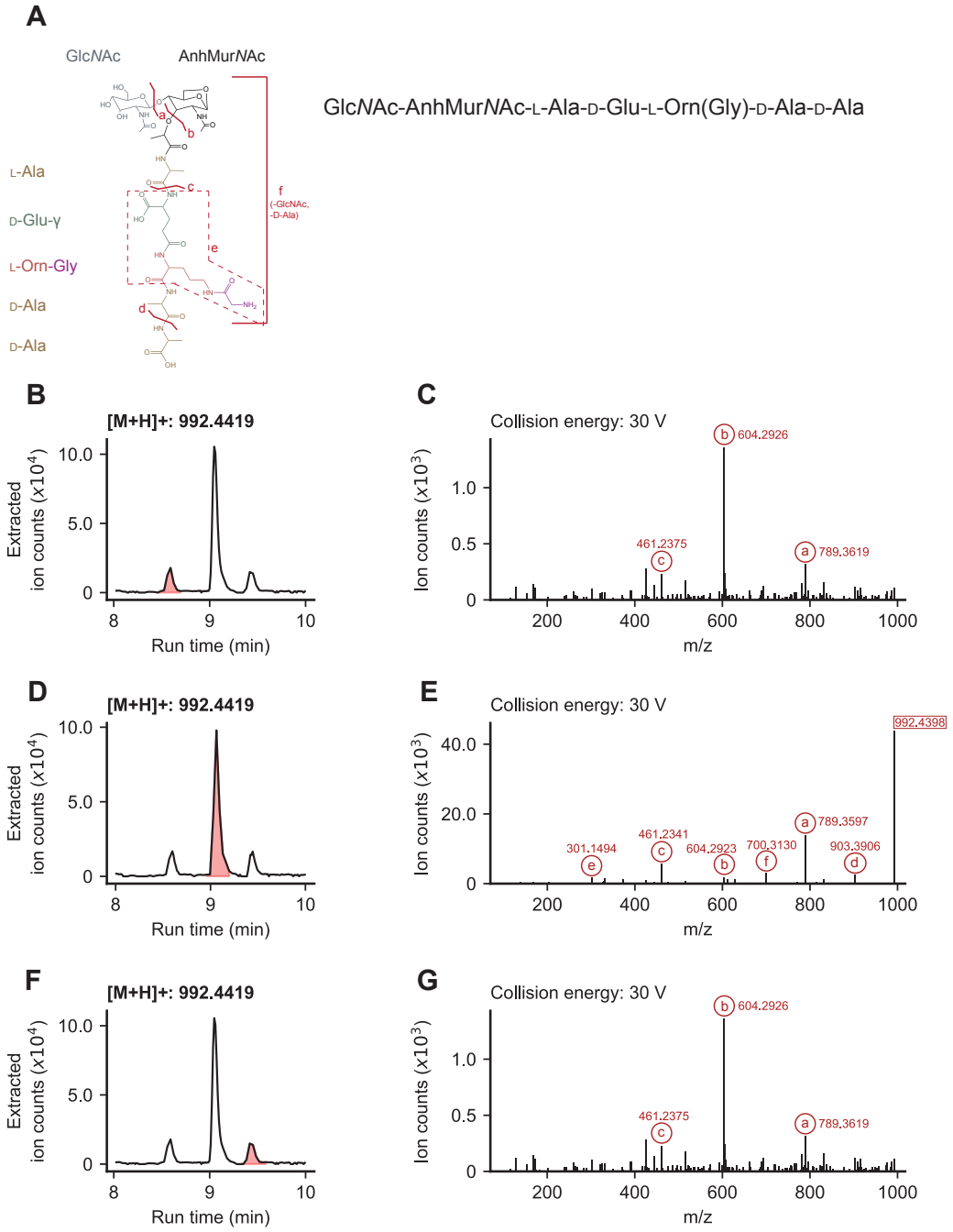

Fig. S3. Fragmentation of PG^{Bb} fragment GlcNAc-AnhMurNAc-L-Ala-D-Glu-L-Orn(Gly)-D-Ala-D-Ala. **A.** Schematic outlining the sugars and amino acids in GlcNAc-AnhMurNAc-L-Ala-D-Glu-L-Orn(Gly)-D-Ala-D-Ala, along with notations of the origin of each identified fragment after MS/MS. **B.** EIC profile of the identified [M+H]+ profile of peak 1, shaded in red. **C.** The MS2 spectrum at the run time where EIC peak 1 in (**B**) is at maximum intensity. **D.** EIC profile of the identified [M+H]+ profile of peak 2, shaded in red. **E.** The MS2 spectrum at the run time where EIC peak 2 in (**D**) is at maximum intensity. **F.** EIC profile of the identified [M+H]+ profile of peak 3, shaded in red. **G.** The MS2 spectrum at the run time where EIC peak 3 in (**F**) is at maximum intensity. For (**C**), (**E**), and (**G**), the collision energies used to fragment this molecule are noted in the titles, and each identified fragment is marked with a letter corresponding to the schematic in (**A**).

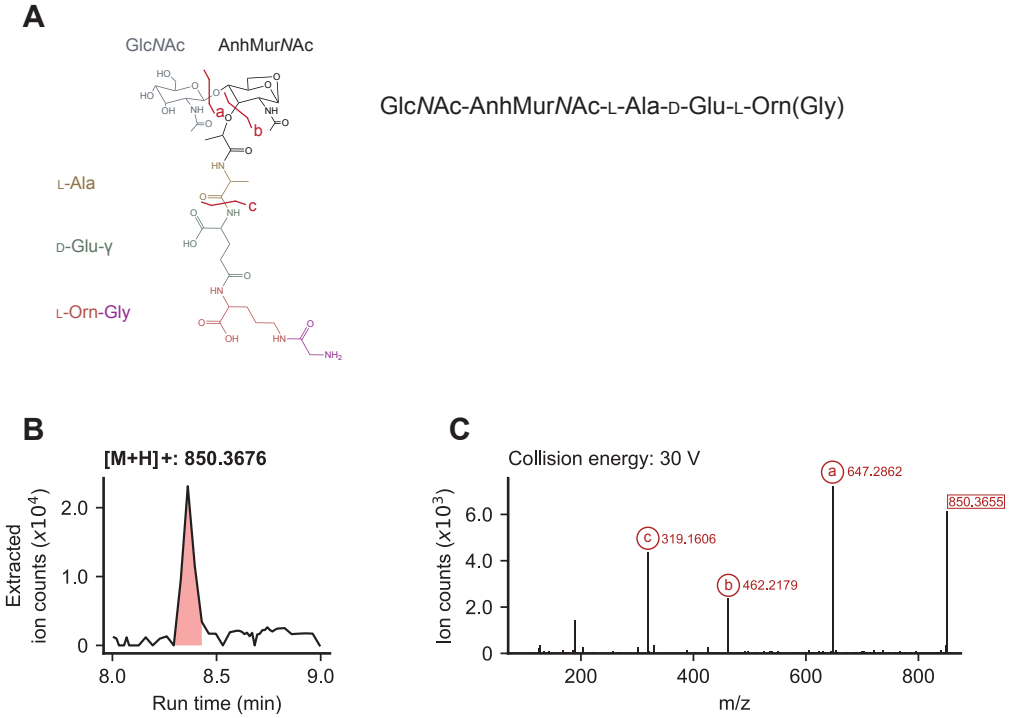

Fig. S4. Fragmentation of PG^{Bb} fragment Glc*N*Ac-AnhMur*N*Ac-L-Ala-D-Glu-L-Orn(Gly). **A.** Schematic outlining the sugars and amino acids in Glc*N*Ac-AnhMur*N*Ac-L-Ala-D-Glu-L-Orn(Gly), along with notations of the origin of each identified fragment after MS/MS. **B.** EIC profile of the identified [M+H]+ profile. The peak of interest is shaded in red. **C.** The MS2 spectrum at the run time where the EIC peak in (**B**) is at maximum intensity. The collision energy used to fragment this molecule is indicated, and each identified fragment is marked with a letter corresponding to the schematic in (**A**).

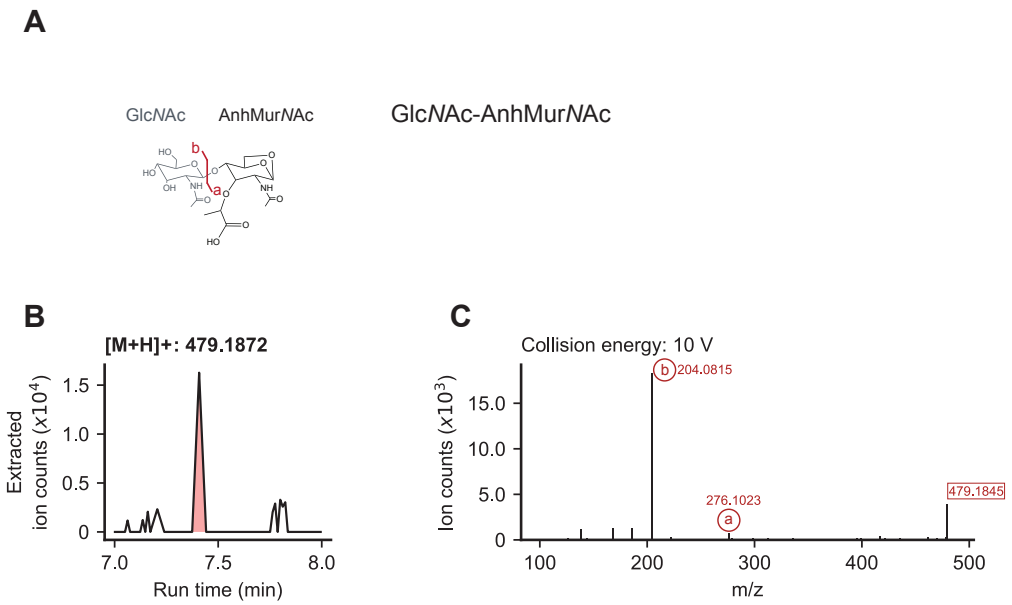

Fig. S5. Fragmentation of PG^{Bb} fragment Glc*N*Ac-AnhMur*N*Ac. A. Schematic outlining each sugar in GlcNAc-AnhMurNAc, along with notations of the origin of each identified fragment after MS/MS. **B.** EIC profile of the identified [M+H]+ profile. The peak of interest is shaded in red. **C.** The MS2 spectrum at the run time where the EIC peak in (**B**) is at maximum intensity. The collision energy used to fragment this molecule is indicated, and each identified fragment is marked with a letter corresponding to the schematic in (**A**).

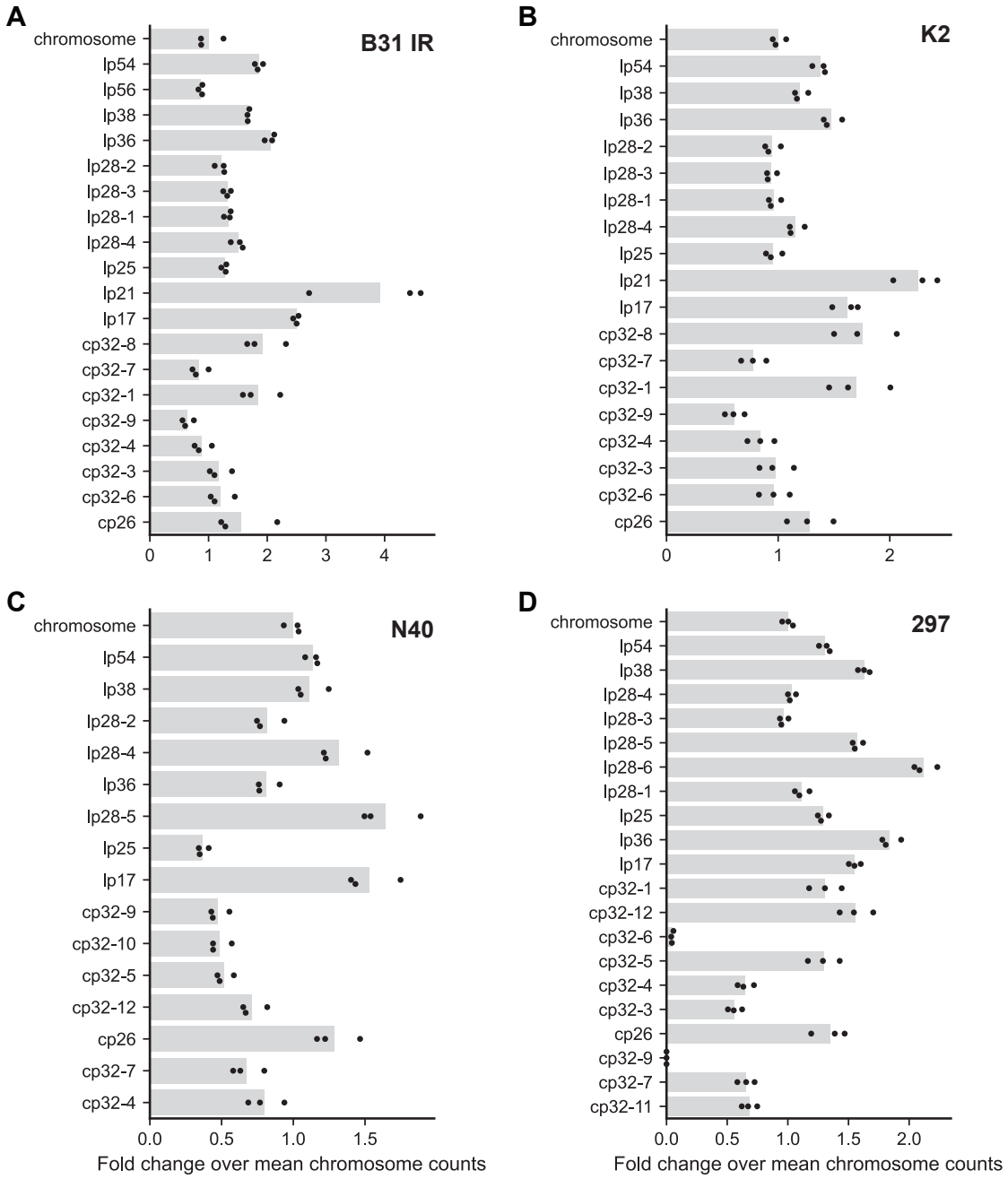

Fig. S6. Plasmid verification in *B. burgdorferi* strains used in the study using whole-genome sequencing. Fold change over mean chromosome read counts for each plasmid present in strains: **A.** B31 IR, **B.** K2, **C.** N40, and **D.** 297. For each strain, a fold change near 0 (< 0.25) indicates that it is missing that plasmid.

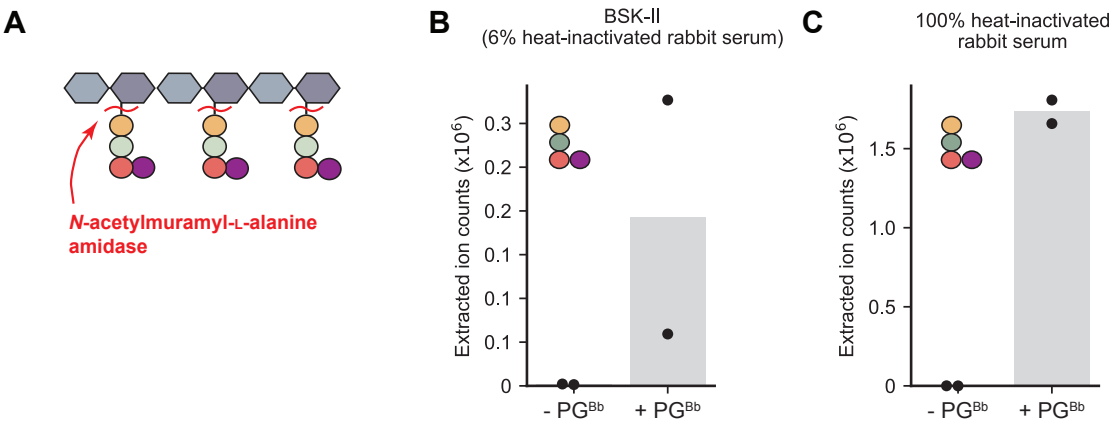

Fig. S7. *N*-acetylmuramyl-L-alanine amidase activity present in BSK-II and heat-inactivated rabbit serum. BSK-II or heat-inactivated rabbit serum was incubated at 37℃ in the presence or absence of purified PG^{Bb} sacculi for 24 h prior to LC-MS. **A.** Schematic of *N*-acetylmuramyl-L-alanine amidase activity when mixed with purified PG^{Bb}. Cut sites by a *N*-acetylmuramyl-L-alanine amidase are shown by red curvy lines. **B.** Digestion in BSK-II. **C.** Digestion in heat-inactivated rabbit serum (100%). For **B**-**C**, plots show the extracted ion count (EIC) for the L-Ala-D-Glu-L-Orn(Gly), the predominant expected digestion product of PG^{Bb} sacculi by a *N*-acetylmuramyl-L-alanine amidase. For both panels, the bar shows the mean and the dots represent the data of two biological replicates of BSK-II media and rabbit sera sourced from different lot numbers.

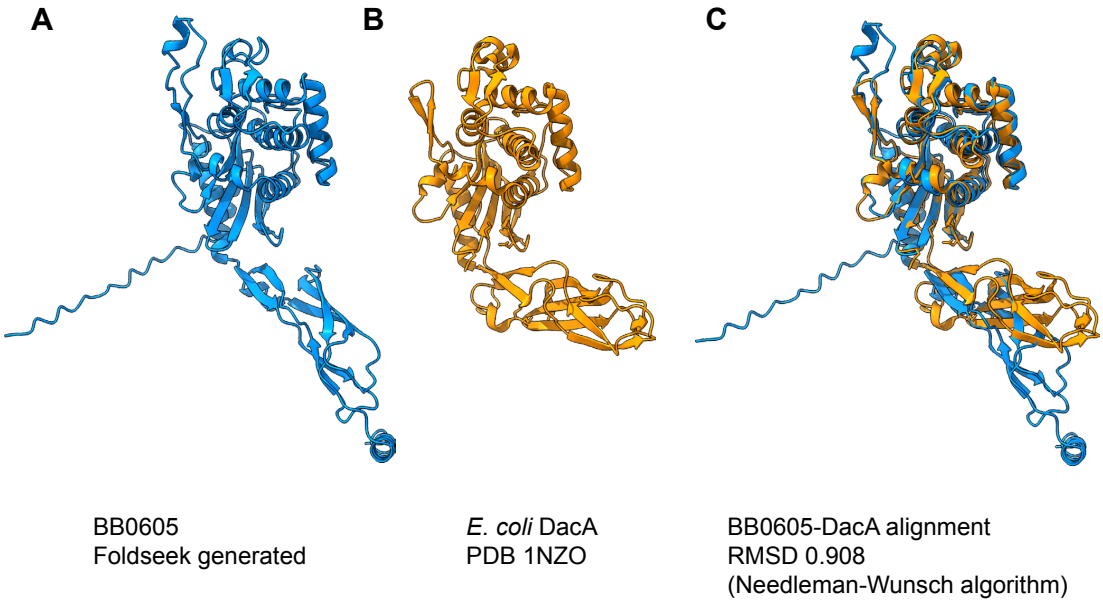

Fig. S8. Structural prediction comparison between *B. burgdorferi* BB0605 and *E. coli* DacA. A. Predicted structure of *B. burgdorferi* BB0605 using Foldseek (109). **B.** Structure of *E. coli* DacA obtained from the Protein Data Bank (PDB) (110, 111). **C.** Alignment of BB0605 and DacA, performed using ChimeraX (112). The root mean square deviation (RMSD) from alignment is presented, along with the alignment algorithm used.

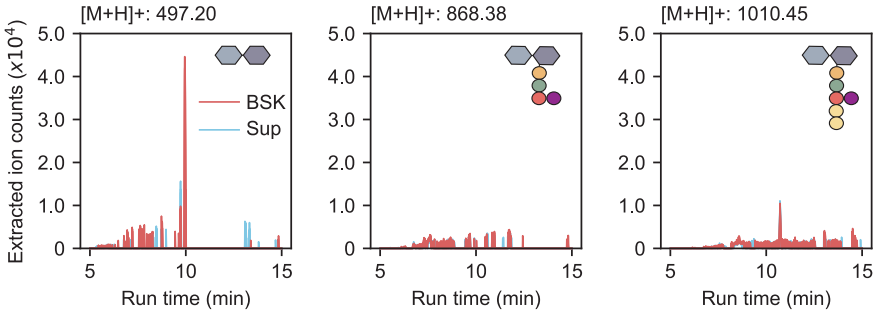

Fig. S9. Assessment of Mur*N*Ac-containing PG species in culture supernatants of *B. burgdorferi* strain K2. Plots showing the extracted ion counts of Glc*N*Ac-Mur*N*Ac, Glc*N*Ac-Mur*N*Ac-L-Ala-D-Glu-L-Orn(Gly), and Glc*N*Ac-Mur*N*Ac-L-Ala-D-Glu-L-Orn(Gly)-D-Ala-D-Ala in culture supernatants (Sup) compared to medium alone (BSK).

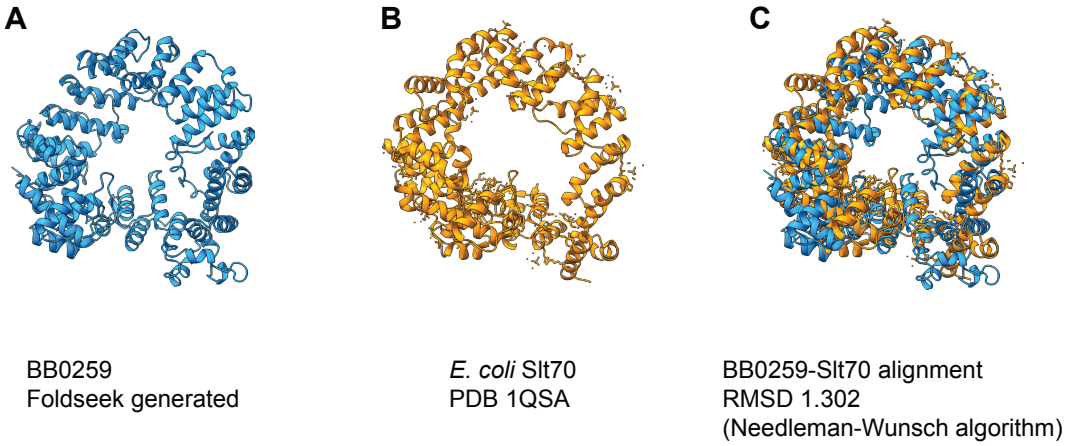

Fig. S10. Structural prediction comparison between *B. burgdorferi* BB0259 and *E. coli* Slt70. A. Predicted structure of BB0259 using Foldseek (109). **B.** Structure of *E. coli* Slt70 obtained from the Protein Data Bank (PDB) (110, 113). **C.** Alignment of BB0259 and Slt70 using ChimeraX (112). The root mean square deviation from alignment is presented, along with the alignment algorithm used.

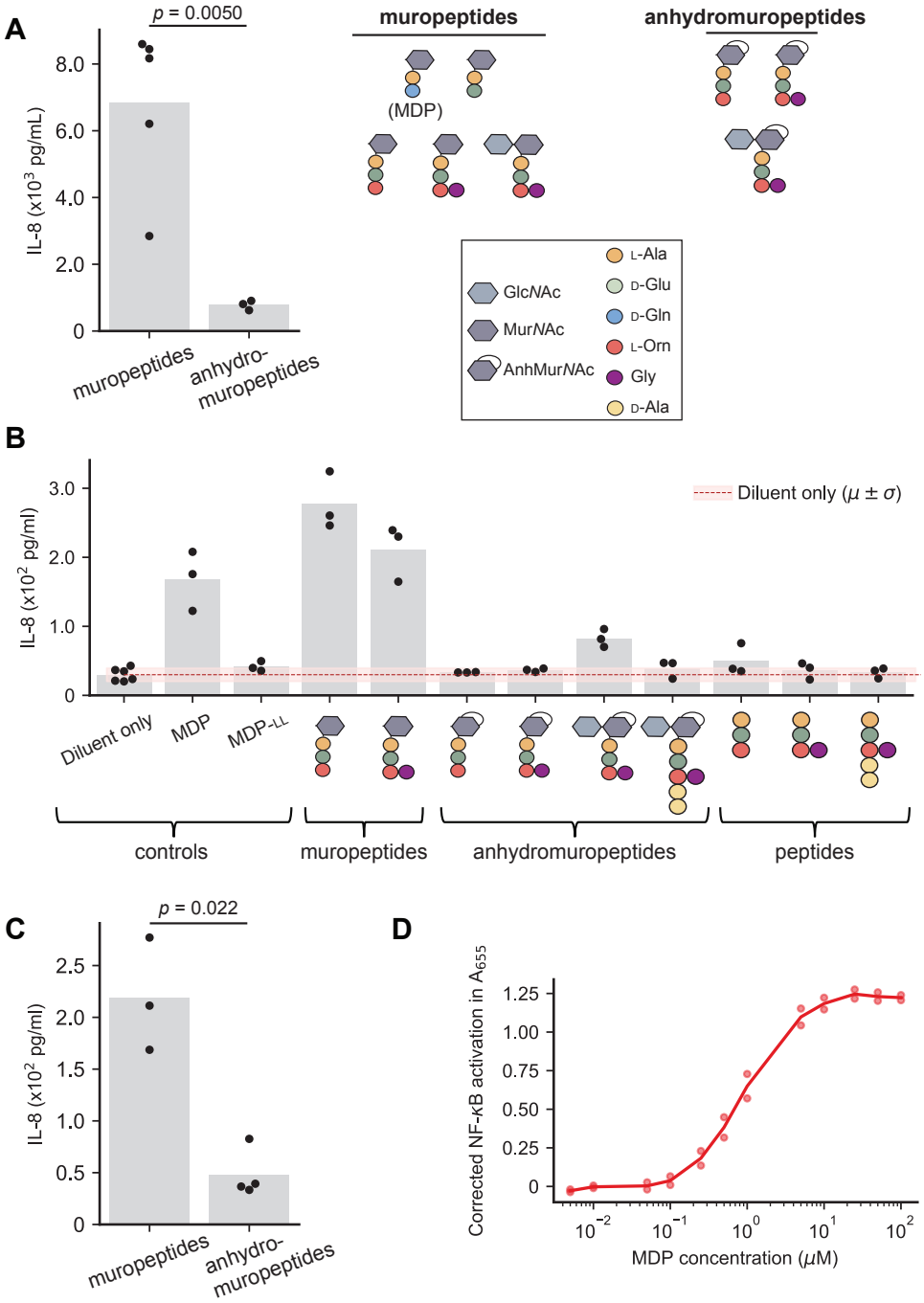

Fig. S11. Stimulation of THP-1 and hNOD2 reporter cells. A. Comparison between Mur*N*Ac-containing and AnhMur*N*Ac-containing species in **Figure 5A**. The schematic of the PG^{Bb} species in each group is shown, along with a legend that defines each chemical moiety. Dots represent the means of each PG^{Bb} compound. Bar heights represent the means for each compound group. The groups were compared using a Welch's t-test to account for different standard deviations and N values. **B.** Plot showing IL-8 production in differentiated THP-1 cells in the presence of the indicated PG^{Bb} fragments. The error bars represent standard deviation of the mean, and bar height represents the mean. Dots represent data from three biological replicates. **C.** Comparison of Mur*N*Ac-containing and AnhMur*N*Ac-containing species in (**B**), including MDP as in (**A**). Dots represent the means of each PG^{Bb} compound. Bar heights represent the means for each compound group. The groups were compared using a Welch's t-test to account for different standard deviations and N values. **D.** Dose-response curve of hNOD2 reporter cells to MDP in MilliQ H2O. The line connects the mean measurements of each concentration, and the dots represent technical replicates.

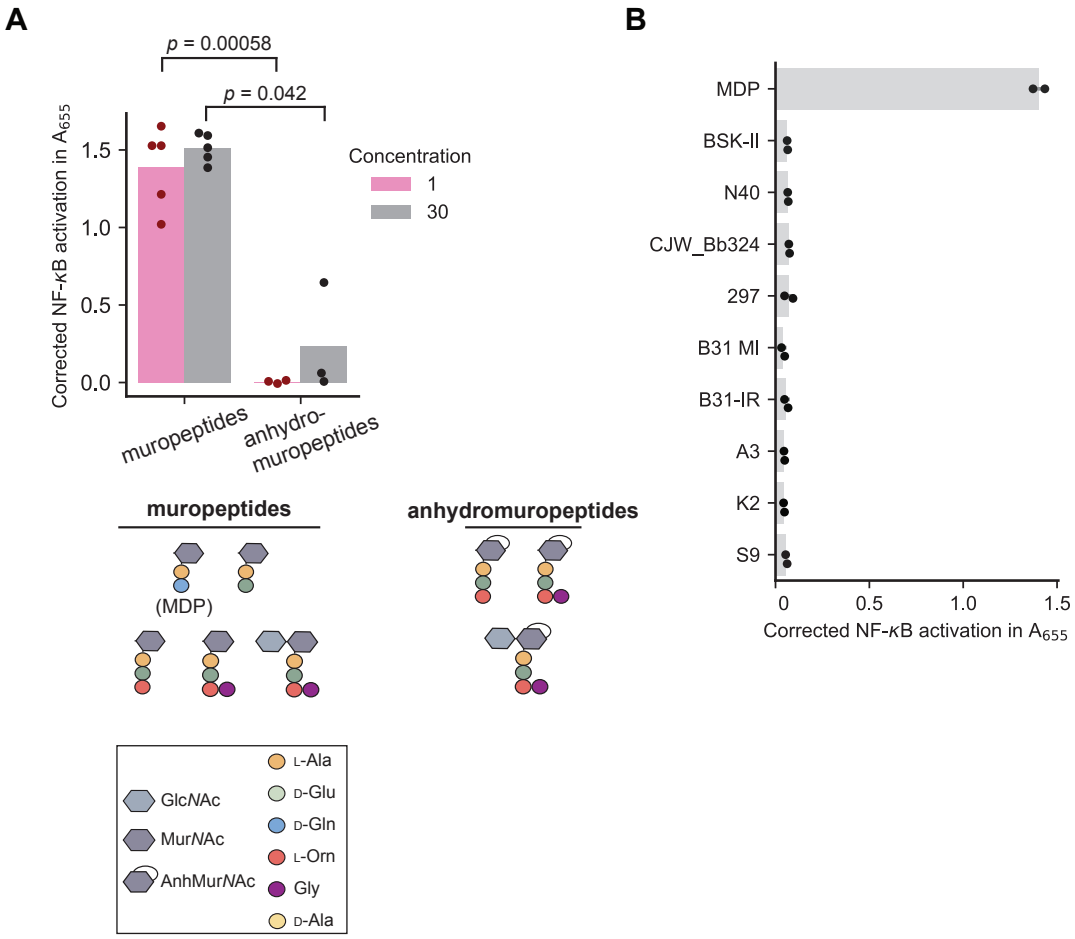

Fig. S12. Absence of detectable stimulation of hNod2 reporter cells by culture supernatants of various *B. burgdorferi* strains. A. NOD2 data from **Figure 5B** with PG^{Bb} grouped based on the presence of a Mur*N*Ac or AnhMur*N*Ac, as shown by the schematics and the legend. Dots represent the means of each PG^{Bb} compound. Bar heights represent the means for each compound group. The lines above the plot show pairwise comparisons between each group using Welch's t-tests to account for different standard deviations and N values. The resulting p-values were adjusted using a Bonferonni correction for multiple comparisons. **B.** Plot showing the SEAP activity of hNOD2 reporter cells (used after fifth passage) following 16-h exposure to 1 μM MDP (positive control) compared to complete BSK-II medium (negative control), or supernatants of cultures in stationary phase for three days. Each dot is a technical replicate, and the height of each bar represents the mean.

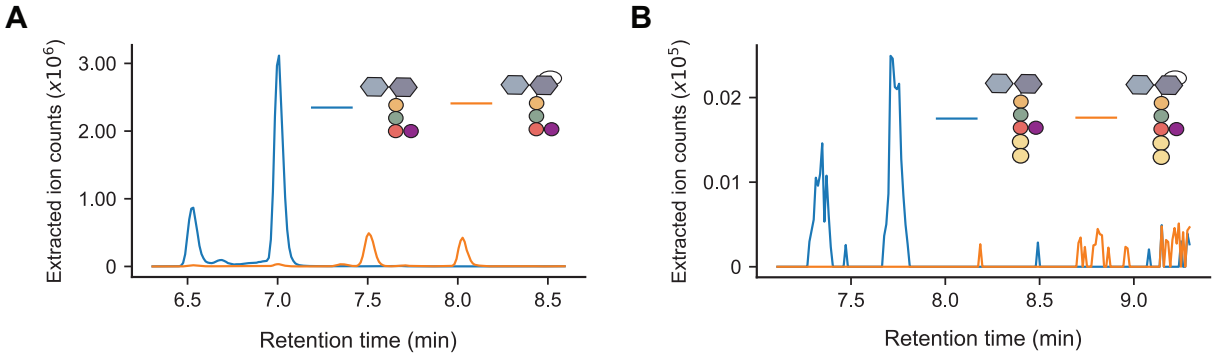

Fig. S13. Ion count profiles of Mur*N*Ac- and AnhMur*N*Ac-containing monomers in PG^{Bb} sacculi isolated from 10-day-old stationary phase cultures of *B. burgdorferi*. PG^{Bb} sacculi were isolated from 10-day-old stationary phase cultures of B31 IR cells and digested with mutanolysin. Digest products were then analyzed by LC-MS. **A.** Extracted ion count profiles for Glc*N*Ac-Mur*N*Ac-L-Ala-D-Glu-L-Orn(Gly) (blue) vs. Glc*N*Ac-AnhMur*N*Ac-L-Ala-D-Glu-L-Orn(Gly) (orange). **B.** Extracted ion count profiles for Glc*N*Ac-Mur*N*Ac-L-Ala-D-Glu-L-Orn(Gly)-D-Ala-D-Ala (blue) vs. Glc*N*Ac-AnhMur*N*Ac-L-Ala-D-Glu-L-Orn(Gly)-D-Ala-D-Ala (orange).

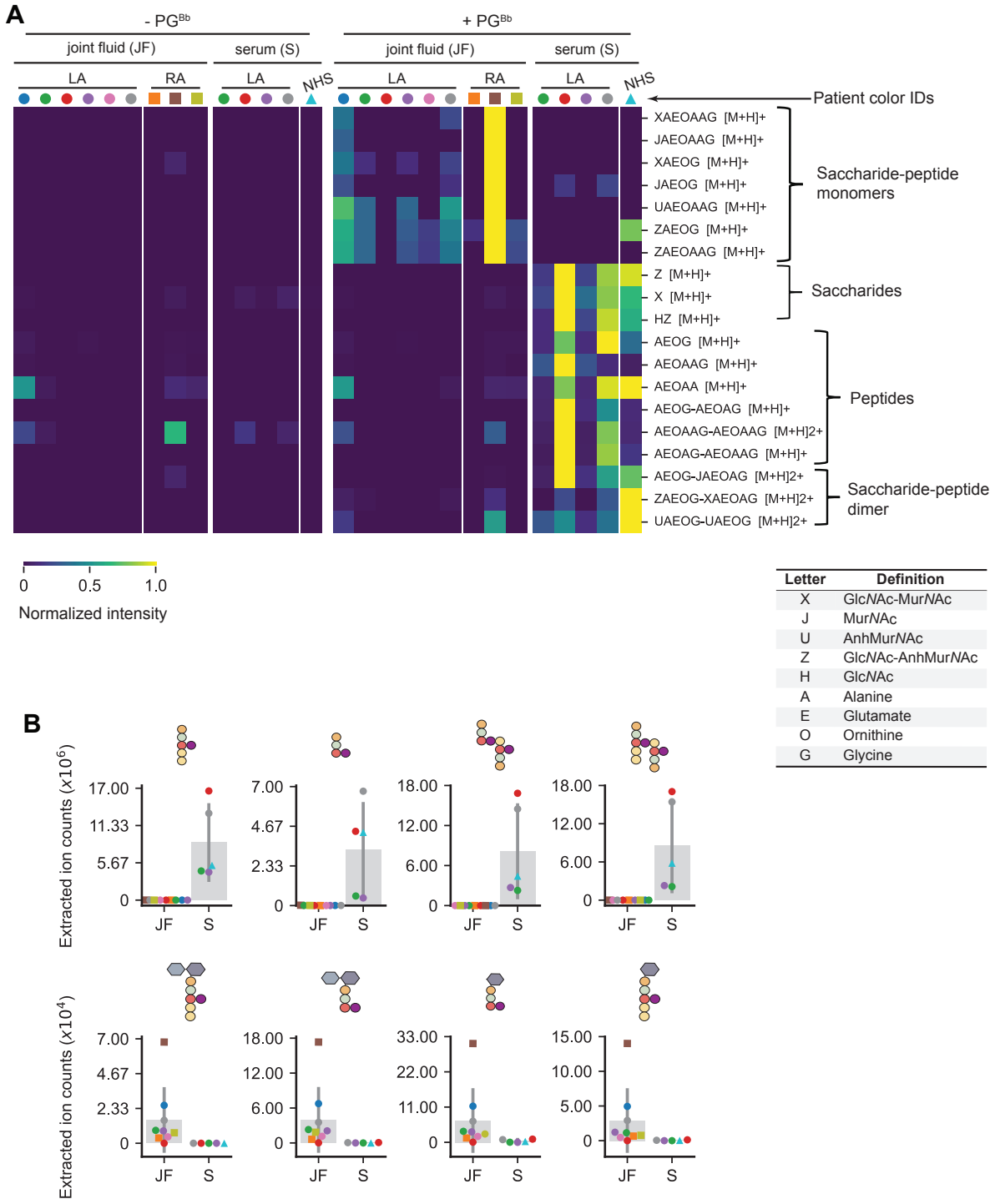

Letter	Definition
X	GlcNAc-MurNAc
J	MurNAc
U	AnhMurNAc
Z	GlcNAc-AnhMurNAc
H	GlcNAc
A	Alanine
E	Glutamate
O	Ornithine
G	Glycine

Fig. S14. Patient joint fluid and serum digestions of purified PG^{Bb} sacculi. This heatmap is similar to **Figure 6A** except that negative control are samples in which no sacculi were added. Samples were incubated with MilliQ H_2O (- PG^{Bb} sacculi) or with PG^{Bb} sacculi (+ PG^{Bb} sacculi) for 6 h, then the resulting reaction products were analyzed by LC-MS. PG^{Bb} species were detected by their predicted [M+H] value (**Supplementary Dataset 1**). All samples were derived from Lyme arthritis patients whose identities (IDs) are color-coded as in **Figure 6A**. The accompanying table contains the key to interpret the PG^{Bb} fragment species in the heatmap. **B.** Representative extracted ion counts for peptide or sugar-peptide conjugate digestion products in serum and joint fluid samples predicted based on their masses. Each dot was derived from integrating the relevant EIC peak. These are the same fragments and analysis as in **Figure 6B**, but with a linear scale on the y-axis.

Table S1. Common PG species referenced within this manuscript. The letter key refers to ths heatmap tables in **Figures 6A** and **S14**. The peptidoglycan fragment masses were generated by summing the masses of each individual subunit and substracting the mass of water with each addition.

№	PG fragment candidate	Letter Key	Calculated mass	Detected mass	Representative image
1	L-Ala-D-Glu-L-Orn(Gly)-D-Ala-D-Ala	AEOAAG	531.2652745	532.2725505 [M+H]+	
2	L-Ala-D-Glu-L-Orn-D-Ala-D-Ala	AEOAA	474.2438112	475.2510872 [M+H]+	
3	Glc*N*Ac-AnhMur*N*Ac-L-Ala-D-Glu-L-Orn(Gly)-D-Ala-D-Ala	ZAEOAAG	991.4345841	992.4418601 [M+H]+	
4	Glc*N*Ac-AnhMur*N*Ac-L-Ala-D-Glu-L-Orn(Gly)	ZAEOG	849.3603575	850.3676335 [M+H]+	
5	Glc*N*Ac-AnhMur*N*Ac	Z	478.1798743	479.1871503 [M+H]+	
6	L-Ala-D-Glu-L-Orn	AEO	332.1695846	333.1768606 [M+H]+	
7	L-Ala-D-Glu-L-Orn(Gly)	AEOG	389.1910479	390.1983239 [M+H]+	
8	Glc*N*Ac-Mur*N*Ac-L-Ala-D-Glu-L-Orn(Gly)	XAEOG	867.3709225	868.3781985 [M+H]+	
9	Glc*N*Ac-Mur*N*Ac-L-Ala-D-Glu-L-Orn(Gly)-D-Ala-D-Ala	XAEOAAG	1009.445149	1010.452425 [M+H]+	
10	Glc*N*Ac-Mur*N*Ac	X	496.1904393	497.1977153 [M+H]+	
11	Mur*N*Ac-L-Ala-D-Glu	JAE	493.1907736	494.1980496 [M+H]+	
12	Mur*N*Ac-L-Ala-D-Glu-L-Orn	JAEO	607.2700869	608.2773629 [M+H]+	
13	Mur*N*Ac-L-Ala-D-Glu-L-Orn(Gly)	JAEOG	664.2915502	665.2988262 [M+H]+	
14	AnhMur*N*Ac-L-Ala-D-Glu-L-Orn	UAEO	589.2595219	590.2667979 [M+H]+	
15	AnhMur*N*Ac-L-Ala-D-Glu-L-Orn(Gly)	UAEOG	646.2809852	647.2882612 [M+H]+	
16	L-Ala-D-Glu-L-Orn[Gly—D-Ala-L-Orn(Gly)-D-Glu-L-Ala]	AEOG-AEOAG	831.4086444	832.4159204 [M+H]+ 416.7115982 [M+H]2+	
17	L-Ala-D-Glu-L-Orn[Gly—D-Ala-L-Orn(Gly)-D-Glu-L-Ala]-D-Ala-D-Ala	AEOAAG-AEOAG	973.482871	974.490147 [M+H]+ 487.7487115 [M+H]2+	

18	Mur*N*Ac-L-Ala-D-Glu-L-Orn(Gly)-D-Ala-D-Ala	JAEOAAG	806.3657768	807.3730528 [M+H]+	
19	AnhMur*N*Ac-L-Ala	UA	346.1376153	347.1448913 [M+H]+ 174.0760837 [M+H]2+	
20	AnhMur*N*Ac-L-Ala-D-Glu-L-Orn(Gly)-D-Ala-D-Ala	UAEOAAG	788.3552118	789.3624878 [M+H]+	
21	Glc*N*Ac-Glc*N*Ac-AnhMur*N*Ac	HZ	681.2592396	682.2665156 [M+H]+	
22	L-Ala-D-Glu-L-Orn[Gly–D-Ala-L-Orn(Gly)-D-Glu-L-Ala-Mur*N*Ac]	AEOG-JAEOAG	1106.509147	1107.516423 [M+H]+ 554.2618494 [M+H]2+	
23	Glc*N*Ac-AnhMur*N*Ac-L-Ala-D-Glu-L-Orn[Gly–D-Ala-L-Orn(Gly)-D-Glu-L-Ala-Mur*N*Ac-Glc*N*Ac]	ZAEOG-XAEOAG	1769.757829	1770.765105 [M+H]+ 885.8861903 [M+H]2+	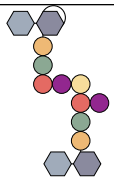

Table S2. ***B. burgdorferi*** **strains used in this study.**

Strain	Relevant genotype/description	Source
B31 MI	Infectious, mouse isolate	(86)
A3	B31 MI *cp9*$^{-}$	(114)
K2	B31-A3-68 lp25[*bbe02*::P_{flgB}-*aphI*] lp56^{-}	(17)
S9	B31-A3-68 lp25[*bbe02*::P_{flgB}-*aphI*] lp56^{-}	(17)
N40	Infectious, tick isolate	(19)
N40 D10/E9	Clonal isolate of N40	(115)
CJW_Bb324	N40 D10/E9 lp25[*bbe02*::*Bbluc-aadA*]	(116)
297	Infectious, patient isolate	(18)
5A18NP1	B31, clone 5A18NP1	(117)
T08TC493	B31, clone 5A18Np1 chr[*bb0605*::*Tn*]	(25)
B31-A	Wild type, noninfectious, high passage	(36)
Δ*bb0531*	B31-A chr[*bb0531*::P_{flgB}-*aphI*]	(36)
Δ*bb0259*	B31-A chr[*bb0259*::P_{flgB}-*aphI*]	(36)
bb0259^{com}	Bb612//pBSV2G-P_{flgB}-BB0259	(36)
B31 MI IR (B31 IR)	B31 MI, clonal isolate	(118)

Table S3. The LC gradient for LC-MS experiments.

Time (min)	A%	B%	Flow (ml/min)
0	100	0	0.2
3	100	0	0.2
7	90	10	0.2
15	80	20	0.2
17	5	95	0.2
17.5	5	95	0.4
19.5	5	95	0.4
20.5	100	0	0.4
24	100	0	0.4
24.5	100	0	0.2
26	100	0	0.2

A: LC-MS-grade H_2O + 0.1% formic acid (Sigma # 1590132500)

B: acetonitrile + 0.1% formic acid (Sigma # 900686)